LASER INTERFEROMETER GRAVITATIONAL WAVE OBSERVATORY
- LIGO -
CALIFORNIA INSTITUTE OF TECHNOLOGY
MASSACHUSETTS INSTITUTE OF TECHNOLOGY

Technical Document LIGO-T960111-A - D 7/26/96

WAVEFRONT SENSOR

DANIEL SIGG

Distribution of this draft:

ASC

This is an internal working note
of the LIGO Project.

California Institute of Technology
LIGO Project - MS 51-33
Pasadena CA 91125
Phone (818) 395-2129
Fax (818) 304-9834
E-mail: info@ligo.caltech.edu

Massachusetts Institute of Technology
LIGO Project - MS 20B-145
Cambridge, MA 01239
Phone (617) 253-4824
Fax (617) 253-7014
E-mail: info@ligo.mit.edu

WWW: http://www.ligo.caltech.edu/

TABLE OF CONTENTS

TABLE OF CONTENTS

1 INTRODUCTION

This document describes the wavefront sensors which were developed for the auto-alignment experiment and which are now used as LIGO prototypes. It outlines the error analysis of the measured wavefront sensing signals, the design of the hardware, the calibration procedure and a possible advanced signal processing scheme.

2 SPECIFICATIONS AND REQUIREMENTS

2.1 Wavefront Sensing and Alignment Specifications

The specifications for wavefront sensing are derived from the ASC (alignment sensing and control) requirements[1]. The mirror angles of the test masses have to be aligned within ~10^{-3} of a beam divergence angle to prevent a degradation of the signal-to-noise ratio of the gravitational wave detection. At the same time, the amount of light which can be used for wavefront sensing should be kept as small as possible, in order not to interfere with the length alignment system. This puts a requirement on the wavefront sensor to be shot noise limited at a fairly low light level and to include a large transimpedance gain. Segmented photodiodes in conjunction with tuned RF circuits and front-end amplifiers are used. Since it is difficult to guarantee a uniform resonance impedance between tuned circuits of different photodiode segments, each photodiode segment is treated as a separate channel. This allows to correct for any unbalance of the individual gains and at the same time to monitor the common mode signal. The down-conversion is performed in 'in-phase' and in 'quad-phase' to reconstruct the full information of the detected RF signal. For applications where only one RF phase is needed a phase shifter for the local oscillator is implemented. To exploit the full capabilities of the wavefront sensors a calibration procedure and a signal processing algorithm has to be established. This will allow to apply calibration corrections in real-time.

2.2 Noise and Error Calculation

Since the wavefront sensing and control implements null servos, one has to distinguish between gain and offset errors in the wavefront sensor. Gain errors do not introduce additional misalignments into the servo system, but rather change the dynamic behavior of the servo. On the other hand, offset errors and noise terms produced in the bandwidth of the servo do misalign the interferometer.

2.2.1 Photodiode Shape

A photodiode which is used to detect alignment signals must be able to measure left/right and up/down asymmetries of the beam. Since a small misalignment signal can be understood as a superposition of TEM_{00} and TEM_{10} mode[2], a possible detection scheme based on the modulation sideband technique measures the combination of the carrier TEM_{00} beating against the TEM_{10} of its sidebands and the carrier TEM_{10} beating against the TEM_{00} of the sidebands. The signal

---

[1] Peter Fritschel, ASC DRD, LIGO-T952007-02-I.

[2] Without loosing any generality the TEM_{01} mode is neglected in this section.

strength S_x expressed as a function of lateral position (x, y) is for both cases proportional to the product of TEM_{00} and TEM_{10} mode:

$$S_x(x, y) = g\frac{4x}{\pi w^3}e^{-\frac{2(x^2+y^2)}{w^2}} \tag{1}$$

where w is the spot size at the detector position and g includes factors accounting for the input light power, the modulation depth, interferometer parameters, the Guoy phase shift between the TEM_{00} and the TEM_{10} at the detector position and the misalignment angle. Since the factor x of eqn. (1) is only present in the beating terms between TEM00 and TEM10 modes and not when they are beating against themselves, a detector that subtracts and integrates over two mirror-symmetric surfaces located left and right of the y-axis, is only sensitive to antisymmetric signals and rejects all symmetric signals. The photodetectors shown in Fig. 1 consist of four segments arranged to form an x-shape. One of them has an additional hole in the center. Two opposite segments are either symmetric along the x-axis or the y-axis and are used to detect horizontal and vertical misalignments, accordingly. The signal for a horizontal misalignment then becomes:

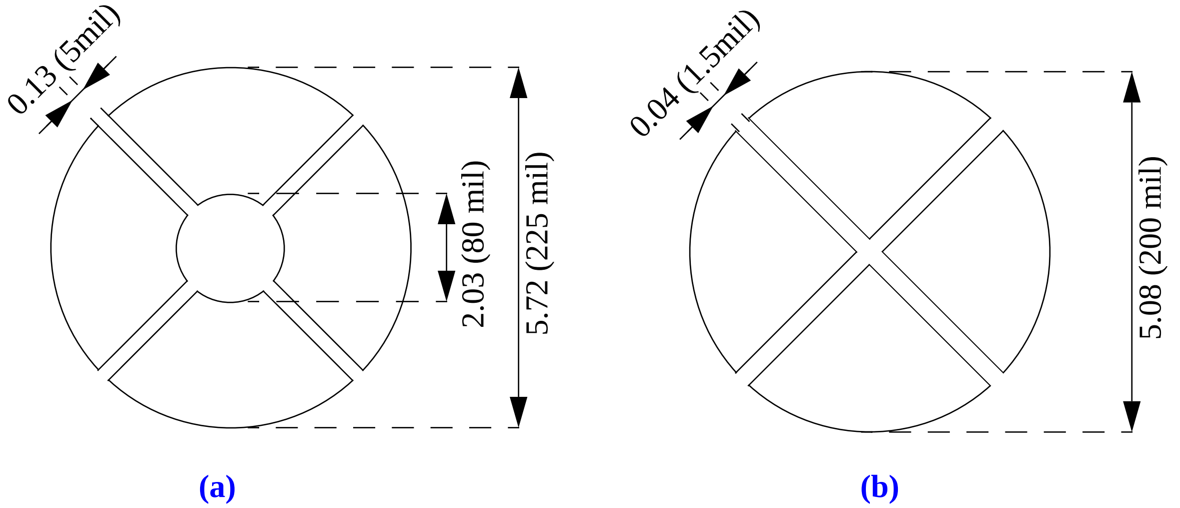

Figure 1: Sensitive area of two four-segment photodiodes; (a) SD 225-23-21-040 and (b) SD 197-23-21-041.

$$S_x \equiv \frac{1}{g}\int_{\Omega} dx\, dy\, S_x(x, y)\, p(x, y) \tag{2}$$

where Ω represents the shape covered by both the left and the right photodetector segment and $p(x,y)$ is a weighting function which takes the sign difference between the left and the right segment into account. For the photodetectors shown in Fig. 1 this equation becomes — if we allow an additional position uncertainty $(\Delta x, \Delta y)$ and an additional orientation error α of the detector:

$$S_x = \frac{4}{\pi} \int_{r_D D/2}^{D/2} dr \left(\int_{-\pi/4+\alpha}^{\pi/4+\alpha} d\varphi - \int_{3\pi/4+\alpha}^{5\pi/4+\alpha} d\varphi \right) \frac{r(r\cos\varphi - \Delta x)}{w^3} e^{-2\frac{r^2 - 2r(\Delta x \cos\varphi + \Delta y \sin\varphi) + \Delta x^2 + \Delta y^2}{w^2}} \tag{3}$$

where D stands for the outer diameter and $r_D D$ for the inner diameter and where we were neglecting the small gap between two adjacent segments.

2.2.1.1 Four-Segment Photodiode with a Center Hole

A list of the dimensions of the photodetector shown in Fig. 1a with their uncertainties can be found in Table 1.

Table 1: Photodetector with a hole:
Dimensions, uncertainties and error propagation coefficients.

Qty.	Description	Value	Error	Unit	$\frac{dS_x}{d\Omega}$	$\frac{d^2S_x}{d\Omega^2}$	$\frac{\Delta S_x}{S_x}$
D	outer diameter	5.715	0.013	mm	0	–0.05	10^{-5}
r_D	inner/outer diameter	0.3556	0.002		–0.69	—	0.003
α	orientation	0	0.05	rad	0	–0.43	0.001
Δx	centering error in *x*	0	0.1	mm	0	–0.19	0.002
Δy	centering error in *y*	0	0.1	mm	0	–0.19	0.002

The beam spot size of the incident beam was chosen, so that a mismatch between the nominal and the physical spot size produces the smallest signal error, i.e.

$$\left.\frac{dS_x}{dw}\right|_{\Delta x = \Delta y = \alpha = 0} = 0 \quad \Rightarrow \quad w_0 = D \sqrt{\frac{r_D^2 - 1}{\log r_D^6}} \tag{4}$$

With the values for the photodetector parameters from Table 1 the maximum signal strength becomes $S_x = 0.4272$ at $w_0 = 2.145$ mm.

By taking the derivatives of eqn. (3) with respect to all detector shape parameters and substituting the spot size with eqn. (4), one obtains the error propagation coefficients for the measured signal. A list of the error propagation coefficients for the above photodetector configuration and the effect on the measured signal S_x is also listed in Table 1. A plot of the misalignment signal as a function of the error variables is shown in Fig. 2.

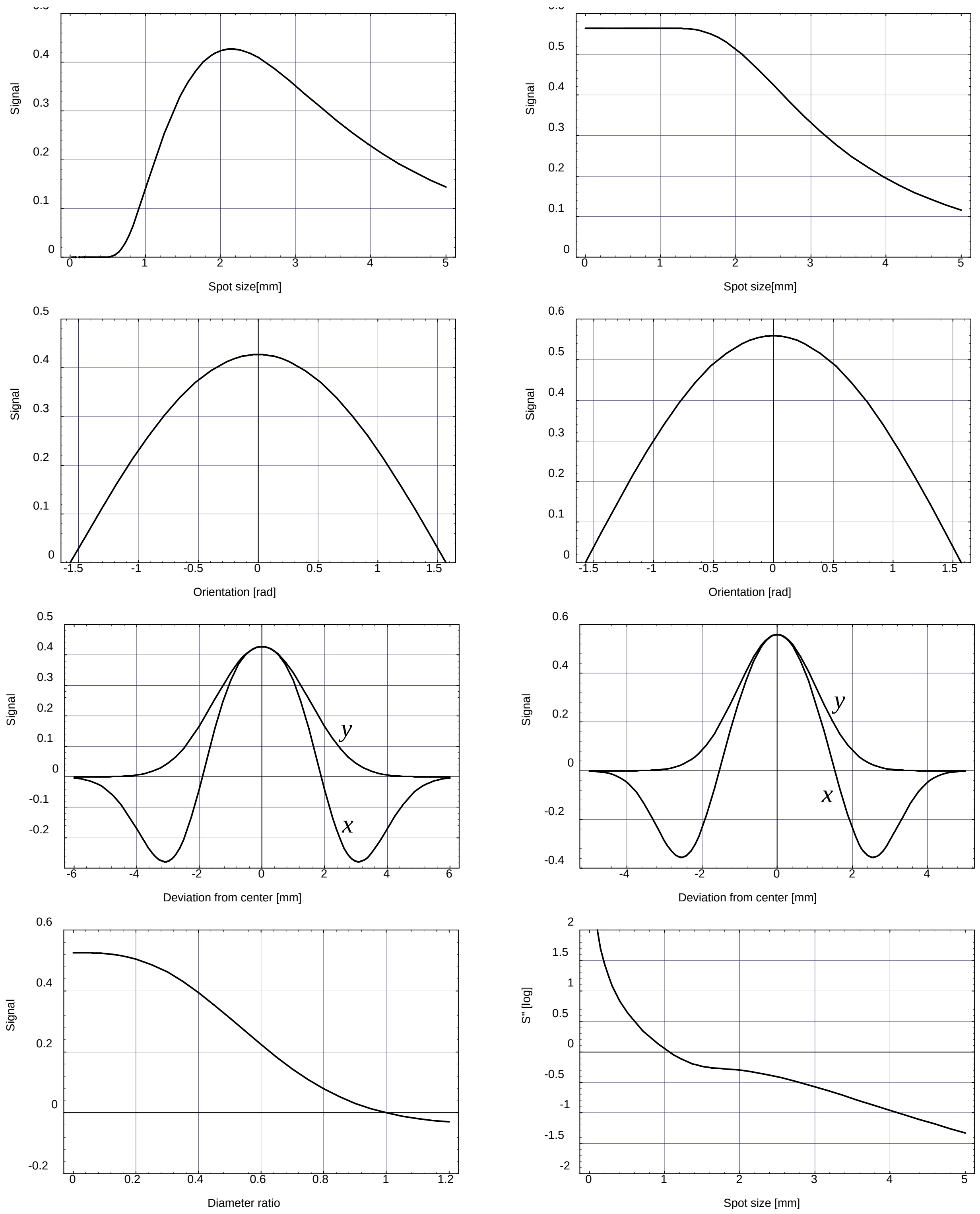

Figure 2: Misalignment signal of photodetectors with holes (left) and without holes (right). Plotted as a function of the beam spot size (1st row), the orientation (2nd), the center position (3rd) and the diameter ratio (4th, left only). The bottom right plot shows the centering sensitivity as a function of the beam spot size.

2.2.1.2 Four-Segment Photodiode without a Center Hole

The four segment photodiode shown in Fig. 1b is a special case of the one with a hole, where the inner diameter is set to zero $r_D = 0$. A list of its dimensions with their uncertainties can be found in Table 2.

Table 2: Photodetector without a hole:
Dimensions, uncertainties and error propagation coefficients.

Qty.	Description	Value	Error	Unit	$\frac{dS_x}{d\Omega}$	$\frac{d^2S_x}{d\Omega^2}$	$\frac{\Delta S_x}{S_x}$
D	outer diameter	5.080	0.013	mm	0.01	–0.02	$2\ 10^{-4}$
α	orientation	0	0.05	rad	0	–0.56	0.001
Δx	centering error in *x*	0	0.1	mm	0	–0.58	0.005
Δy	centering error in *y*	0	0.1	mm	0	–0.51	0.005

The smaller the beam spot size on the photodetector is the larger the signal and the less important the uncertainty of the spot size is. However, the sensitivity to centering errors also increases with a smaller beam spot size. The beam spot size was therefore chosen, so that 99% or more of a misalignment signal is detected on the photodetector and only 1% or less outside the its sensitive area, i.e.

$$\left.\frac{dS_x}{dw}\right|_{\Delta x = \Delta y = \alpha = 0} = 0.99\left.\frac{dS_x}{dw}\right|_{D\to\infty,\ \Delta x = \Delta y = \alpha = 0} \qquad (5)$$

With the values for the photodetector parameters from Table 2 the signal strength is $S_x = 0.99/\sqrt{\pi}$ at $w_0 = 1.508$ mm.

By taking the derivatives of eqn. (3) with respect to all detector shape parameters and substituting the spot size calculated with eqn. (5), one obtains the error propagation coefficients for the measured signal. A list of the error propagation coefficients for the above photodetector configuration and the effect on the measured signal S_x is also listed in Table 2. A plot of the misalignment signal as a function of the error variables is shown in Fig. 2.

2.2.1.3 Correcting for Centering Errors

The centering uncertainty dominates the error of the measured signal. An other effect which wasn't discussed until now is the loss of common mode rejection when the beam is not exactly centered on the photodetector. Demanding even more precision for centering seems unrealistic, since the requirement is already rather strict. An other possibility to improve both the centering error and the common mode rejection ratio is to measure the position of the beam on the photodetector with the DC photocurrent produced in each segment and then correct for it. We define a quantity which measures the asymmetry between opposite photodiode segments and is independent of the amount of light hitting the detector:

$$A_x = \frac{S_{dc}^{+} - S_{dc}^{-}}{S_{dc}^{-} + S_{dc}^{+}} \equiv \frac{\Delta x}{w} a_x \qquad (6)$$

where A_x stands for the right/left-asymmetry, S_{dc}^{-} is the dc photocurrent in the left detector segment and S_{dc}^{+} is the dc photocurrent in the right segment. We write this asymmetry as the beam position Δx over the beam spot size w multiplied by a constant a_x coming from the integration of the light over the photodetector. Similarly, we define a_y which stands for the vertical asymmetry. Assuming that most of the light hitting the photodetector, when the interferometer is aligned, is in the TEM_{00} mode, we can readily calculate a_x; $a_x = 2.803$ for the photodetector with the hole and $a_x = 2.242$ for the one without the hole (as a comparison: $a_x = 2\sqrt{2/\pi}$ for half-plane detector). Fig. 3 plots these asymmetry coefficients as a function of the beam spot size on the photodetector.

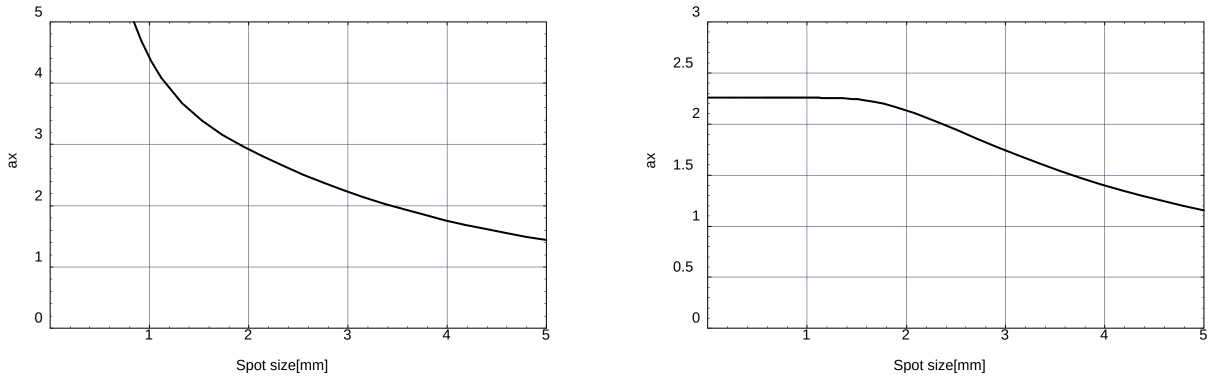

Figure 3: Asymmetry coefficient as a function of the beam spot size.
left: photodetector with hole and right: photodetector without hole.

A contamination of TEM_{10} mode in the incident beam will lead to an error in the determination of the beam position. By using

$$w\frac{d}{dx}\left|\mathrm{TEM}_{00}(x,y)\right|^2 = 2\,\mathrm{Re}(\mathrm{TEM}_{00}(x,y)\mathrm{TEM}_{10}(x,y)) \qquad (7)$$

one can show that for small contaminations $\Delta x/w = \mathrm{Re}\ f$ with f the amplitude ratio between the TEM_{10} and the TEM_{00} mode. Especially, at the dark port of an interferometer the measurement of the center position with the dc photocurrent might have additional uncertainties, since a large fraction of the light power is contained in higher order modes. For this case the intrinsic uncertainty in the determination of the beam position might be as high as 10% of the beam spot size.

The dependence of the misalignment signal as defined in eqn. (2) on the beam centering is only quadratic in the deviation of the beam axis from the center of the photodetector; i.e. the correction factor f_x^{cen} reads:

$$f_x^{\mathrm{cen}} = \left(1 + \frac{1}{2S_x}\frac{d^2 S_x}{d\Delta x^2}\left(\frac{A_x}{a_x}w\right)^2 + \frac{1}{2S_x}\frac{d^2 S_x}{d\Delta y^2}\left(\frac{A_y}{a_y}w\right)^2\right) \tag{8}$$

An uncertainty of 10% of the spot size in determining the beam center position would lead to approximately an uncertainty of 0.5% in the correction factor (see Tables 1 and 2).

For a discussion of the effect of beam centering on the common mode rejection ratio see section 2.2.6.

2.2.2 Beam Propagation (Telescope)

A laser beam leaving the interferometer usually has the wrong spot size and the wrong Guoy phase shift for an optimal detection of a misalignment signal with a wavefront sensor of the shape described in the previous section. The misalignment signal can be written as:

$$S(\eta, w) = g_{\mathrm{ifo}}\cos(\eta - \eta_0)S_x(w) \tag{9}$$

where S_x is defined in eqn. (2), g_{ifo} is a constant accounting for the signal strength at the interferometer output, η_0 is the Guoy phase at the interferometer output, η the Guoy phase shift added by the telescope and w the spot size on the detector. Assuming we are interested in $S(\eta_0, w_0)$ with w_0 the optimal (nominal) beam spot size as defined in eqns. (4) or (5), then the total error of the detected misalignment signal χ is the sum of the intrinsic (design) error in η and w and the errors coming from the uncertainties of the positions z_i and the focal lengths f_i of the telescope lenses.

$$\chi = \chi_I + \chi_z + \chi_f \tag{10}$$

$$\chi_I = \left|2\sin^2\left(\frac{\eta - \eta_0}{2}\right)\right| + \left|g_w^{(1)}(w - w_0)\right| + \left|g_w^{(2)}\frac{(w - w_0)^2}{2}\right| \tag{11}$$

with $$g_w^{(1)} = \frac{1}{S(\eta_0, w_0)}\frac{d}{dw}S(\eta_0, w)\bigg|_{w_0} \quad \text{and} \quad g_w^{(2)} = \frac{1}{S(\eta_0, w_0)}\frac{d^2}{dw^2}S(\eta_0, w)\bigg|_{w_0} \tag{12}$$

The second term in eqn. (11) introduces the second derivative for the error calculation, since the first derivatives are either zero or negligible for the photodetectors described in section 2.2.1. They are $g_w^{(1)} = 0$ and $g_w^{(2)} = -0.77\,\mathrm{mm}^{-2}$ for the detector with the hole and $g_w^{(1)} = -0.07\,\mathrm{mm}^{-1}$ and $g_w^{(2)} = -0.34\,\mathrm{mm}^{-2}$ for the one without the hole at their nominal beam spot sizes.

If one defines functions $\eta(z_i, f_i)$ and $w(z_i, f_i)$ which describe the Guoy phase shift of the telescope and the beam spot size on the detector as a function of the positions z_i and focal lengths f_i of the telescope lenses, the relative error of the detected misalignment signal can be obtained as follows:

$$\chi_z = \sum_{i=1}^{n} \left\{ \left(\frac{d\eta}{dz_i}\right)^2 \frac{\Delta z_i^{\,2}}{2} + \left| g_w^{(1)} \frac{dw}{dz_i} \Delta z_i \right| + \left| g_w^{(2)} \right| \left(\frac{dw}{dz_i}\right)^2 \frac{\Delta z_i^{\,2}}{2} \right\} \qquad (13)$$

χ_f can be easily obtained from eqn. (13) by replacing z_i with f_i throughout the equation. The quantities Δz_i and Δf_i denote the uncertainties of the lenses in the position and focal length, respectively. One has to use the second derivatives again, since the first ones are either identically zero or very small.

The above equations can also be used to optimize the design of a telescope. By minimizing χ with respect to the positions and focal lengths of the telescope lenses — taken into account the additional constraints imposed by the available space and by the availability of lenses — the best telescope configuration can be determined. For the photodetector without hole (described in section 2.2.1.2) the error due to an uncertainty of the beam spot size is negligible, if $w < 1.5\,\text{mm}$. However, the sensitivity to centering errors increases dramatically for smaller spot sizes. It is then recommended to design the telescope for a nominal spot size of $w_0 \approx 1.0\,\text{mm}$ and to use $g_w^{(1)} = 0$ and $g_w^{(2)} \approx -1\,\text{mm}^{-2}$ in the minimization process.

2.2.3 Shot Noise

For the aligned interferometer the shot noise is mainly coming from the TEM_{00} mode, since its intensity dominates over the other modes (this is even true for the dark port because of the sidebands). We write the r.m.s. photocurrent due to shot noise of the TEM_{00} mode as:

$$i_{rms}^{SN} = \sqrt{2q\varepsilon S_{00}\, f_{BW}} \qquad (14)$$

with q the elementary charge, ε the efficiency of the photodetector, S_{00} the intensity of the TEM_{00} mode over the area of the photodetector and f_{BW} the bandwidth of the alignment servo system. The measured intensity of the TEM_{00} mode is a function of the input laser power P, a coefficient coming from interferometer configuration k_{ifo}^{00}, the fraction of the output light f_{split} which is guided towards the wavefront sensor and the fraction of the incoming light k_{PD}^{00} which hits the photodetector:

$$S_{00} = P\, k_{ifo}^{00}\, f_{\text{split}}\, k_{PD}^{00} \qquad (15)$$

For the photodetector with the hole (described in section 2.2.1.1) the fraction of detected light is $k_{PD}^{00} = 0.3048$, i.e. 31% of the light in the TEM_{00} mode is absorbed by the two horizontal segments of the photodiode, whereas for the photodetector without the hole (described in section 2.2.1.2) $k_{PD}^{00} = 0.4983$.

An interesting quantity is the misalignment angle which would correspond to the shot noise current level induced by the average light power on the photodetector (as defined in eqn. (14)).

$$i_{rms}^{SN} \equiv \varepsilon S_{10} \qquad (16)$$

where S_{10} is now the misalignment signal produced by a tilted optical component which is misaligned by an (normalized) angle α_{SN}; to first order:

$$S_{10} = P\Gamma k^{10}_{ifo} f_{\text{split}} k^{10}_{PD} \alpha_{SN} \tag{17}$$

where Γ is the modulation depth, k^{10}_{ifo} is the alignment coefficient due to the interferometer configuration and k^{10}_{PD} is the ratio of the signal which is detected by the existing photodetector over the signal which would be measured by a photodetector consisting of two half planes — split along the y-axis — which are subtracted from each other. For the photodetector with the hole (section 2.2.1.1) the signal as defined in eqn. (2) is 0.4272, whereas the corresponding signal on a half-plane detector would be $\sqrt{2/\pi}$. Thus, the signal ratio becomes $k^{10}_{PD} = 0.5354$. For the photodetector without the hole (section 2.2.1.2) $k^{10}_{PD} = 0.99/\sqrt{2}$.

Substituting eqns. (14), (15) and (17) into eqn. (16) gives:

$$\alpha_{SN} = \frac{\sqrt{2q\ f_{BW}\ k^{00}_{ifo} k^{00}_{PD}}}{\sqrt{\varepsilon P f_{\text{split}}}\ \Gamma k^{10}_{ifo} k^{10}_{PD}} \tag{18}$$

Since all the parameters except f_{split} (and to some extend f_{BW}) are fixed, putting a requirement on the misalignment angle induced by the shot noise, i.e. $\alpha_{SN} < \alpha_{max}$, will immediately translate into a requirement for the amount of light which has to be split off for the wavefront sensor, i.e. $f_{\text{split}} > f_{min}$. If f_{min} becomes larger than 100% (or the maximum fraction of light which is available for the wavefront sensor), the shot noise will prevent the requirement on the tolerated misalignment angle from being met.

The effect of a particular shape of the photodetector on of the signal-to-noise ratio compared to a simple half-plane detector can be calculated with:

$$\left.\frac{S}{N}\right|_{\text{4-segment PD}} \div \left.\frac{S}{N}\right|_{\text{half-plane}} = \frac{k^{10}_{PD}}{\sqrt{k^{00}_{PD}}} \approx 1 \tag{19}$$

Meaning that both proposed photodetectors neither improve nor worsen the signal-to-noise ratio significantly.

2.2.4 Analog Electronics

2.2.4.1 Noise

The front-end electronics consists of a coil which is mounted in parallel to the photodiode — forming a resonant circuit at the modulation frequency — and a very low noise preamplifier. Including the current and the voltage noise of the preamplifier (CLC425), $i_N = 1.6\ \text{pA}/\sqrt{\text{Hz}}$ and $v_N = 1.05\ \text{nV}/\sqrt{\text{Hz}}$, the total electronic noise becomes:

$$e_N = \sqrt{\frac{4kT}{R} + i_N^2 + \left(\frac{v_N}{R}\right)^2} \tag{20}$$

where R denotes the impedance of the resonance circuit. A plot is shown in Fig. 4. The noise spectrum below $R = 10\,\mathrm{k\Omega}$ is dominated by the Johnson noise.

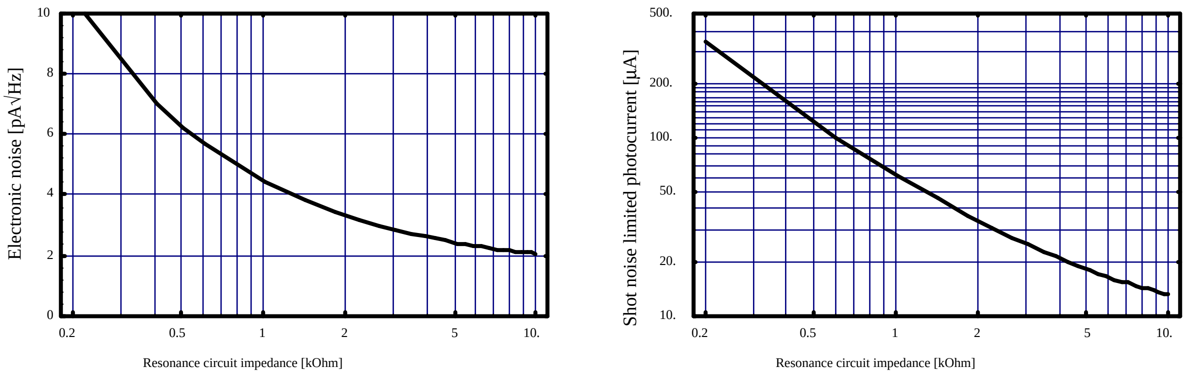

Figure 4: The noise produced by the RF front-end electronics (left) and the shot noise limited photocurrent (right) as a function of the resonance circuit impedance.

The spectral density of the photocurrent due to shot noise is given by:

$$i_{SN} = \sqrt{2qI_{PD}} \tag{21}$$

where q is the elementary charge and I_{PD} the average photocurrent. Setting the electronic noise equal to the shot noise level yields the shot noise limited photocurrent, above which the shot noise dominates over the electronic noise (see Fig. 4). For typical resonant circuit impedance values 50 µA photocurrent (or 0.25 mW of green light) is enough to guarantee a shot noise limited detection.

2.2.4.2 Down-Conversion

A mixer can be understood as a multiplication device which multiplies the signal applied to the RF port with a square wave signal which is in-phase with the LO reference signal and which oscillates between –1 and 1. If the signal at the RF port is a superposition of the modulation frequency and its harmonics

$$S_{RF} = \sum_{n=1}^{\infty} A_n \cos(n\omega t - \phi_n) \tag{22}$$

and if we write the square well signals of two independent mixers as real and imaginary part of one LO reference signal

$$S_{sqw} = \frac{4}{\pi}\sum_{n=1}^{\infty}\frac{1}{2n-1}(\cos((2n+1)\omega t - \Phi_I) \pm i\sin(2n+1)\omega t - \Phi_Q) \tag{23}$$

then the down-converted signal becomes

$$S_{DC} = g_{\otimes} \sum_{n=1}^{\infty} A_{2n-1} \frac{4}{\pi} \frac{1}{2n-1} \frac{1}{2} (\cos(\phi_{2n-1} - \Phi_I) \pm i \sin(\phi_{2n-1} - \Phi_Q)) \tag{24}$$

with Φ_I and Φ_Q the phase of the two LO signals and with $g_{\otimes}$ the mixer gain ($\pi/2$ for the AD831 mixer IC from Analog Device). From the above equations one sees that only harmonics which are odd multiples of the modulation frequency are down-converted. If we write Φ_I and Φ_Q as the sum of a common phase shift Φ plus terms coming from common and differential phase errors, $\Delta\Phi_c$ and $\Delta\Phi_c$, respectively,

$$\Phi_I = \Phi + \Delta\Phi_c + \frac{\Delta\Phi_d}{2} \quad \text{and} \quad \Phi_Q = \Phi + \Delta\Phi_c - \frac{\Delta\Phi_d}{2} \tag{25}$$

the imaginary part of eqn. (23) becomes a square well signal which is 90° out of phase in respect to the real part signal — either leading (minus sign) or lagging (plus sign). If we are now assuming that the interesting signal with amplitude A_1 is in the ‘in-phase’ $\phi_1 = \Phi$ and that no harmonics of the modulation frequency are present in the RF input signal, the error in the down-converted signal becomes

$$\frac{\Delta S_{DC}}{S_{DC}} = \sqrt{\left(\frac{\Delta g_{\otimes}}{g_{\otimes}}\right)^2 + \left(\frac{\Delta\Phi_c^2}{2}\right)^2 + \left(\frac{\Delta\Phi_d^2}{8}\right)^2} \tag{26}$$

If there is a potentially dangerous signal with amplitude $\bar{A}_1$ in the ‘quad-phase’ $\bar{\phi}_1 = \Phi + \pi/2$, a DC offset error in S_{DC} might result:

$$\Delta S_{DC}^{ofs} = \frac{2}{\pi} g_{\otimes} \bar{A}_1 \left(\Delta\Phi_c + \frac{\Delta\Phi_d}{2}\right) \tag{27}$$

2.2.4.3 Transimpedance Gain

The signal i_{PD}^{RF} produced in the photodiode by an incident laser beam is a current, whereas the down-converted signal $S_{\text{meas.}}$ measured after the mixer is a voltage. Therefore, one can write the total gain in the electronics as a transimdedance gain:

$$S_{\text{meas.}} = R_{\text{gain}} i_{PD}^{RF} = R_{\text{gain}} \varepsilon S_{\text{light}} \tag{28}$$

with ε the efficiency of the photodiode and S_{light} the intensity of the modulated light signal on the photodetector. Because the signals of each photodiode segment are preamplified and down-converted separately, the misalignment signal S_{10} as defined in eqn. (17) is proportional to the difference of the two down-converted signals from right and left photodiode segment — $S_{\text{meas.}}^{\text{right}}$ and $S_{\text{meas.}}^{\text{left}}$, respectively — divided by the transimpedance gain and the efficiency of the photodiode:

$$S_{10} = \frac{S_{\text{meas.}}^{\text{right}}}{\varepsilon R_{\text{gain}}^{\text{right}}} - \frac{S_{\text{meas.}}^{\text{left}}}{\varepsilon R_{\text{gain}}^{\text{left}}} \tag{29}$$

Since for a pure misalignment signal the signals produced in the right and left photodiode segment have opposite signs, the error in S_{10} can be written as:

$$\frac{\Delta S_{10}}{S_{10}} = \sqrt{\left(\frac{\Delta\varepsilon}{\varepsilon}\right)^2 + \frac{1}{4}\left[\left(\frac{\Delta S^{\text{right}}_{\text{meas.}}}{S^{\text{right}}_{\text{meas.}}}\right)^2 + \left(\frac{\Delta S^{\text{left}}_{\text{meas.}}}{S^{\text{left}}_{\text{meas.}}}\right)^2 + \left(\frac{\Delta R^{\text{right}}_{\text{gain}}}{R^{\text{right}}_{\text{gain}}}\right)^2 + \left(\frac{\Delta R^{\text{left}}_{\text{gain}}}{R^{\text{left}}_{\text{gain}}}\right)^2\right]} \tag{30}$$

2.2.5 Quantization Noise

The down-converted signals are digitized with an ADC (analog-to-digital converter) and read into a computer for further processing. Since the ADC has a finite resolution, the digitalization introduces a quantization noise. Under the assumption that the round-off errors are statistically distributed (might require a dither) and that appropriate anti-aliasing filters are used, the quantization noise is a white noise source. If the resolution (1 bit) of the ADC is given by ΔS_Q, the spectral density of the quantization noise N_Q reads

$$N_Q^2 = \frac{\Delta S_Q^2}{6\, f_S} \tag{31}$$

with f_S the sampling frequency.

2.2.6 Common Mode Rejection

A common RF signal on two opposite photodetector segments does in first order not produce any differential signal which could be interpreted as a misalignment signal. However, if the electronic gains in the two photodetector segments aren’t exactly equal, or if the photodetector is not precisely centered to the incident laser beam, a common mode signal on the photodetector can produce a differential signal. We define the common mode rejection ratio (CMRR) as the ratio of the measured common signal over the measured differential signal for an arbitrary common mode excitation:

$$\text{CMRR} = \left|\frac{S^{\text{right}}_{\text{CM}} + S^{\text{left}}_{\text{CM}}}{S^{\text{right}}_{\text{CM}} - S^{\text{left}}_{\text{CM}}}\right| \tag{32}$$

An infinity value for the CMRR would indicate a perfect rejection of all common mode, whereas a CMRR of, say, 40 dB would mean that 1% of the common mode signal would appear in the differential signal.

The CMRR due to an unbalance of the electronic gains can be calculated from eqn. (28) assuming that the photocurrent in the two segments are equal:

$$\text{CMRR}_{\text{gain}} = \left|\frac{R^{\text{right}}_{\text{gain}} - R^{\text{left}}_{\text{gain}}}{R^{\text{right}}_{\text{gain}} + R^{\text{left}}_{\text{gain}}}\right|^{-1} \tag{33}$$

For example, an individual gain calibration of 1% would lead to a CMRR of 43 dB. An other cause of loss in common mode rejection is a centering error of the photodetector. Assume that the common mode RF signal is caused by a beating of a carrier TEM_{00} mode against the TEM_{00}

mode of its sidebands — e.g. the longitudinal cavity error signal — then moving the photodetector horizontally out of its center will increase the signal on one photodiode segment and will decrease it on the opposite one, resulting in a differential signal. The calculation of this effect is completely analogous to the calculation of the asymmetry effect due to the DC light (see section 2.2.1.3). Using eqn. (6) one obtains:

$$\mathrm{CMRR}_{\mathrm{cen}} = \left|A_x^{-1}\right| = \left|a_x^{-1}\frac{w}{\Delta x}\right| \tag{34}$$

The measurement of the beam position on the photodetector Δx can be used to improve the common mode rejection by adding a correction term $\Delta S_{10}^{\mathrm{corr.}}$ to the measured misalignment signal S_{10}:

$$\Delta S_{10}^{\mathrm{corr.}} = -\left(\frac{S_{\mathrm{meas.}}^{\mathrm{right}}}{\varepsilon R_{\mathrm{gain}}^{\mathrm{right}}} + \frac{S_{\mathrm{meas.}}^{\mathrm{left}}}{\varepsilon R_{\mathrm{gain}}^{\mathrm{left}}}\right)\frac{\Delta x}{w}a_x \tag{35}$$

An interesting quantity is angular error corresponding to given longitudinal misalignment, when the common mode rejection isn't perfect. If we use the angular misalignment signal as defined in eqn. (17) and if we define the longitudinal signal on the photodetector as follows:

$$S_{\Delta l} = P\,\Gamma k_{ifo}^{\Delta l}\, f_{\mathrm{split}}\, k_{PD}^{00}\, k\,\Delta l \tag{36}$$

with $k_{ifo}^{\Delta l}$ the longitudinal sensitivity of the interferometer, k the wave vector of the laser light and Δl the longitudinal deviation, then the corresponding angle becomes

$$\alpha_{\Delta l} = \frac{1}{\mathrm{CMRR}}\,\frac{k_{PD}^{00}}{k_{PD}^{10}}\,\frac{k_{ifo}^{\Delta l}}{k_{ifo}^{10}}\,k\,\Delta l \tag{37}$$

It can be shown that for a simple non-degenerate Fabry-Perot interferometer the factor $k_{ifo}^{\Delta l}/k_{ifo}^{10}$ is of the order of the finesse of the cavity. Hence, the best cure against a coupling of longitudinal motion into angular alignment is a tight length locking servo.

2.2.7 Higher Order Modes

Until now we were only considering the RF signals coming from a beating between TEM10 and TEM00 modes. However, there is an infinite number of possible combinations between higher order modes that can produce a signal on the photodetector which could be misinterpreted as a misalignment signal. If this signal is also generated by a misalignment, it will in first order not give any false information and the null servo will still work fine. But, if this higher order modes are produced by an intrinsic error of the mirrors, they may introduce a dc offset into the servo loop. Generally, one can write the signals coming from other higher order modes as:

$$S_x^{all} = \sum_{mn,\,kl} g_{mn,\,kl}\cos\eta_{mn,\,kl}\left|E_{mn}^{cr}\right|\left|E_{kl}^{sb}\right| \tag{38}$$

where $\left|E_{mn}^{cr}\right|$ and $\left|E_{kl}^{sb}\right|$ are the amplitudes of the carrier and sideband modes of order *mn* and *kl*, respectively. $\eta_{mn,\,kl}$ is the phase difference between these two modes at the photodetector position and $g_{mn,\,kl}$ are factors taking the shape of the photodetector into account. They are defined analogous to the ones from eqns. (2) and (3) for the misalignment signal:

$$g_{mn,\,kl} = \int_{\Omega} dx dy \mathrm{TEM}_{mn}(x, y)\mathrm{TEM}_{kl}(x, y)p(x, y) \tag{39}$$

where Ω represents the sensitive area of the photodetector and $p(x, y)$ is a weighting function which determines for the sign of the integrand. Due to the axissymmetry of the Hermite-Gaussian modes the following rules apply for half-plane detectors and the ones from section 2.2.1:

$$g_{mn,\,kl} = 0 \quad \text{if} \quad \begin{cases} mk \text{ is even} \\ nl \text{ is odd} \end{cases} \tag{40}$$

and
$$g_{mn,\,kl} = g_{kl,\,mn} = g_{ml,\,kn} = g_{kn,\,ml} \tag{41}$$

A list of all distinct and non-zero values for $g_{mn,\,kl}$ up to modes of third order are given in Table 3. The list includes values for a half-plane photodetector, the 4-segment detector with central hole (section 2.2.1.2) and the 4-segment detector without the hole (section 2.2.1.2). From this table one can see that other mode combinations are able to produce rather large signals, if their contribution to the laser beam coming from the interferometer is significant.

Table 3: Photodetector Sensitivity to Higher Order Modes.

Modes		Photodetector		
mn	kl	half-plane	4-segment with hole	4-segment w/o hole
10	00	$\sqrt{2/\pi} = 0.798$	0.427	0.559
20	10	$\sqrt{1/\pi} = 0.564$	0.453	0.558
11	01	$\sqrt{2/\pi} = 0.798$	0.214	0.269
02	10	0	–0.151	–0.205
30	00	$-\sqrt{1/3\pi} = -0.326$	–0.087	–0.134
30	20	$\sqrt{3/2\pi} = 0.691$	0.149	0.462
30	02	0	0.041	0.111
21	11	$\sqrt{1/\pi} = 0.564$	0.253	0.421
12	00	0	–0.151	–0.205
12	20	0	–0.142	–0.097
12	02	$\sqrt{2/\pi} = 0.798$	0.122	0.195
03	11	0	–0.162	–0.179

3 HARDWARE DESCRIPTION

3.1 Telescope

TBD.

3.2 Sensor Head

Sensor head data sheet

Parameter	Condition	Min.	Typ.	Max.	Unit
PHOTODIODE[1]					
Bias Voltage				75	V
Breakdown Current				5	mA
Capacitance	bias voltage: 75V		12		pF
Series Resistance	$f = 25$ MHz		25	100	Ω
Size of Segment	5.72 (OD); 2.03 (ID)		5.4		mm^2
DIODE CURRENT					
Transimpedance	DC	9.99	10.0	10.1	kΩ
Bandwidth			50		kHz
Offset Error	DC at output		1.5	10	mV
RF CIRCUIT					
Tuning Frequency Range		10		70	MHz
Q	$f_T = 25$ MHz, no notch		13		
Notch Frequency Range	both notches	10		120	MHz
Notch Attenuation	$f_T = 25$ MHz, $f_N = 50$ MHz		25		dB
Transimpedance	$f_T = 25$ MHz, no notch, low gain		70		kΩ
High Gain Setting	$f_T = 25$ MHz, no notch		+20		dB
Electronic Output Noise	$f_T = 25$ MHz, no notch, low gain		100		nV/$\sqrt{\text{Hz}}$
Shot Noise Limit. Photocurrent	$f_T = 25$ MHz, no notch		50		µA
Crosstalk	$f_T = 25$ MHz, high gain[2]			–50	dB
Output Impedance			50		Ω
POWER SUPPLY					
+12V	range: +10V to +15V			260	mA
–12V	range: –10V to –15V			160	mA
PHYSICAL					
Size	RF enclosure	152 (H) × 76 (W) × 54 (D)			mm^3

1. Advanced Photonix SD 225-23-21-040 (with hole)
   Advanced Photonix SD 197-23-21-041 (without hole).
2. The crosstalk improves by 20 dB for low gain setting.

This section describes the wavefront sensor head electronics[1] as shown on the attached diagram (see Appendix C.1). The earlier design used gain changing in both the RF and diode-current-sensing sections, but with the elimination of gain changing in the DC part, the design became relatively simple. The three parts of the design are an RF tuning section, an RF amplifier and a diode-current-sensing section.

3.2.1 RF Tuning

The fundamental tuned circuit consists of the capacitance of the photodiode U1 resonating with L7. In the diagram, the resonant frequency is given as 20 MHz, but the actual frequency may lie anywhere between 20 and 70 MHz. Diode U1 has a capacitance determined by the bias voltage; for the particular diode used, the capacitance will be about ~10 pF with a 75 V bias. This bias is applied through an LC filter consisting of C21, C22 and L1, a filter intended to decouple the bias supply from the RF signal. Since the value of C22 is large compared to the diode capacitance, its value will have little effect upon the resonant frequency. Two other capacitors, C28 and C29, are involved with detecting the dc component of diode current, but they too have large values compared to the diode capacitance so can also be neglected. From an RF standpoint, the circuit can be treated as a shunt-tuned circuit consisting of the capacitance of U1 in parallel with the inductance of L7. L2-C23 and L6-C30 are two series resonant circuits intended to reduce the second and third harmonics of the fundamental frequency.

At a nominal dc diode current of 0.5 mA, the RF or ac signal current is assumed to have a value of 0.8 µA r.m.s., or 1.13 µA peak. This current appears in parallel with the tuned circuit, so the peak voltage is a function of the shunt resistance, which is in turn a function of the circuit Q. If we assume a tuned circuit capacitance of 10 pF and a Q of 10, then at 20 MHz this shunt resistance will be 7958 Ohms, giving a peak signal voltage of 8.99 mV or an r.m.s. value of 6.36 mV.

3.2.2 Shot and Thermal Noise

A significant amount of shot noise is generated by the dc photodiode current. This noise has an r.m.s. value per $\sqrt{Hz}$ of $I_{shot} = \sqrt{2QI}$, which at our nominal diode current of 0.5mA is 12.6 pA/$\sqrt{Hz}$. There is also some thermal noise from the shunt resistance whose r.m.s. value per $\sqrt{Hz}$ is given by $I_{thernal} = \sqrt{kT/R}$. For 7958 Ohms, this is 1.44pA/$\sqrt{Hx}$, which is sufficiently small compared to the shot noise that it can be ignored. If we assume a tuned circuit Q of 10 at 20 MHz, then the bandwidth is 2 MHz, so the total shot noise appearing across the tuned circuit will be 141.8 µV.

3.2.3 Tunable Inductors

Three of the inductors shown on the circuit diagram are shown as adjustable. However, since the exact operating frequencies can lie anywhere in the range of 20 to 70 MHz (and two and three times this for harmonics), we need inductors that can be easily modified rather than prewound inductances. This means that we have to wind our own coils as we determine the operating frequencies, so we need coil forms rather than prewound coils.

---

[1] Designed and written by William E. Earle (EDF, Boston University), November 1995.

There are many manufacturers of prewound coils, but relatively few suppliers of bare coil forms. One such manufacturer is Lodestone Pacific from whom I have obtained a sample kit of adjustable coil forms in various sizes. These coil forms are fully shielded, which is an important requirement if we are to minimize coupling between channels, and come in sizes down to 0.3 inches square. The Q's of the coils are generally above 50, and can be optimized by selecting wire and cores according to an application selection guide. If the fundamental tuned circuit should have a Q considerably higher than 10, it may be desirable to reduce it by adding series resistance R1. Although a high Q is desirable from a signal-to-noise standpoint, it also increases the sensitivity of phase change to frequency shift, an undesirable effect.

The Lodestone coil forms that seem reasonable for this application are

- L31-6-CT-B-4. Used for 2.0 to 30MHz.
- L31-10-CT-B-4. Used for 10 to 100MHz.
- L31-17-CT-B-4. Used for 20 to 200MHz.

These forms are 0.3 inch square and use very small removable bobbins. It should be noted that these are very small coil assemblies that will require patience and care for proper assembly. These coil forms are quite inexpensive, in the vicinity of $1 each.

3.2.4 The RF Amplifier

Assuming a maximum full-scale output of 10 dBm into 50 Ohms, we get a maximum voltage output of 1.0 V peak. However, since there is to be an overrange of 30 dB, which is a factor of 31.6, we end up needing a 31.6 mV peak signal under normal operating conditions. Since our nominal signal from the tuned circuit is 8.99 mV peak, determined previously, the output amplifier needs a voltage gain of 31.6/8.99 = 3.52. It is customary practice when using an op-amp to drive a 50 Ohm line to use a series resistance of 50 Ohms, and if we do this we actually need a gain of $2 \times 3.52 = 7.04$. This is sufficiently close to the minimum gain of 10 for a low-noise CLC425 amplifier, that we might as well just use a gain of 10 rather than the calculated 7.04.

3.2.5 Amplifier Noise

The CLC425 has a voltage noise component, a current noise component and a thermal noise component from the amplifier feedback resistor. The CLC425 is specified to have a voltage noise of 1.05×10^{-9} V per $\sqrt{Hz}$ and a current noise of 1.6×10^{-12} A per $\sqrt{Hz}$.

At a gain of 10, the CLC425 has a bandwidth of 170 MHz, so the total voltage noise at its input will be 13.7 mV. The current noise flows through the tuned circuit shunt resistance of 7958 Ohms, so it sees a bandwidth of only 2 MHz. Thus the voltage at the amplifier input due to the current noise will be 18.0 mV. The thermal noise due to the feedback resistor network of 90 Ohms is 15.9 mV using a 170 MHz bandwidth. Adding the three noise sources gives an amplifier input noise of 27.6 mV. Note that the shot noise calculated previously was 141.8 mV, so the amplifier noise is a negligible part of the total noise. Using the previously determined signal level of 6.36 mV, then the signal-to-noise ratio is 33 dB. Of course, the use of a narrower output bandwidth will increase this value.

3.2.6 Diode Current Measurement

The dc component of the diode current is sensed by a transconductance amplifier whose negative input terminal is held at virtual ground potential. Thus, the current sensing does not introduce any offset voltage that would change the diode bias and circuit tuning and RF phase. Of course, for this approach to work, the amplifier must be stable with the relatively large capacitive load, C28, that is needed to provide a low impedance path for the RF current flowing through L7.

Some amplifiers are designed to be stable with capacitance up to 1000 pF, but few can stand higher capacitive loads. Fortunately, there is at least one amplifier, the AD847 (and its dual version, the AD827) that is stable with any capacitive load. This amplifier also has a low offset voltage, a low offset current and a 35 MHz bandwidth. (It is also readily available and not merely a data sheet.) It does have a limited gain of about 3500, though, so should not be used without considerable feedback to maintain gain stability.

Capacitor C29 serves the two functions of providing a relatively low impedance RF path (for the same reason as C28) and in combination with R5 setting the bandwidth of the current-sensing circuit. Unfortunately, maintaining a reasonable bandwidth with a large value for C29 means a low value of R5, but this reduces the gain and increases the effect of the error from the amplifier offset voltage. With the compromise values shown on the diagram, the bandwidth is 48 kHz and the output is 1.66 V for a 0.5 mA diode current. The maximum amplifier offset voltage is 2 mV, but the typical is only 0.5 mV, so the error is of the order of 0.1% or less. The maximum offset current error is 300 nA with a typical value of 50 nA. Using the maximum value, a 1.0 mV error would occur, less than 0.1% of the full-scale signal.

A second stage of amplification with a gain of 3 brings the final output to 5 V for a diode current of 0.5 mA. This stage includes a 160 kHz lowpass network to remove any remaining traces of the RF signal without affecting the 48 kHz bandwidth. The current offset error from this second amplifier is negligible but the voltage offset error will be the same as for the input stage. This means that the total error could exceed 0.1%, but typically this won't be the case.

Another approach using a composite amplifier consisting of a very low offset, narrow bandwidth amplifier combined with a wider bandwidth amplifier was considered, but the increase in circuit complexity did not seem worthwhile. If an error of 0.1% or so is acceptable, then I prefer the suggested approach; if we really need a smaller error, then we need to consider a more complicated circuit.

3.2.7 Power Supplies

It seems reasonable to use supplies of ±12 V and on-board regulators to provide the ±5 V needed by the CLC425's. In order for the AD827's to provide a +5 V output, these amplifiers can use the unregulated +12 V supply.

3.3 Demodulator Board

Demodulator board data sheet

Parameter	Condition	Min.	Typ.	Max.	Unit
LOCAL OSCILLATOR					
Frequency Range		12		100	MHz
Input Level		–20		+20	dBm
Input Resistance			50		Ω
PHASE SHIFTER					
Input Level Range		–5		+5	V
Conversion Factor			1.3		V/rad
I/Q CLOCK					
Phase Difference[1]	adjustable	+85		+95	degree
PLL Phase Noise	at 1 kHz (estimated)		–140		dBc
RF INPUT					
Number of Channels			5		
Frequency Range		12		100	MHz
Maximum Input Level			+10		dBm
1 dB Compression Point			+10		dBm
Crosstalk	$f = 50$ MHz			–80	dB
Input Resistance			50		Ω
OUTPUT					
Output Voltage Range		–10		+10	V
Gain	down-conversion		14.1		V/V
Bandwidth	double pole Butterworth filter		10		kHz
Output Voltage Noise	at 1 kHz		150		$\mathrm{nV}/\sqrt{\mathrm{Hz}}$
Output Offset Error	adjustable		10		mV
Output Offset Error Gradient	0°C < T < 50°C	+0.8	+1.2	+1.6	mV/°C
POWER SUPPLY					
+5.2V	range: +4.9V to +5.3V			1000	mA
–5.2V	range: –5.0V to –5.3V			1500	mA
+24V	range: +20V to +30V			550	mA
–24V	range: –20V to –30V			550	mA
PHYSICAL					
Size	VME compatible	double europe (6U)			
Cooling	air flow	requires a fan			

[1] Sign of quad-phase is jumper selectable.

The demodulator board[1] has an RF part (see Fig. 5) and a low frequency part. The RF part performs the actual demodulation of the measured light intensity. It is itself divided into two parts: the local oscillator part which provides the demodulation clock signals and the mixer part which performs the down-conversion. There are 5 RF channels for the down-conversion which is done both into in-phase and quad-phase. The low frequency part of the demodulator board takes the down-converted signals and amplifies and filters them. The schematics can be found in Appendix C.2.

3.3.1 Mixer

For each of the 5 RF input signals 2 Gilbert-cell mixers are used (AD831) to obtain the down-converted in-phase and quadrature-phase signals. The RF input signals are fed directly into the mixer inputs using only one 50Ω resistor to GND for each RF channel. The necessary demodulation clock signals are provided by a local oscillator (see next section) which produces 2 master clock signals which are 90° out of phase. The down-converted output signal of the mixer is low-pass filtered (corner frequency at about 300 kHz), before it is fed into the on-chip amplifier which is set to unity gain. A passive RC-filter is then used at its output to remove any remaining trace of the up-converted signal, before the output signal is further amplified with a low noise OpAmp and filtered again with a 2nd order Butterworth which has a corner frequency of 10 kHz. Since this type of mixer has a fairly large DC offset error at the down-converted output, a potentiometer is used for initial zero-adjustment.

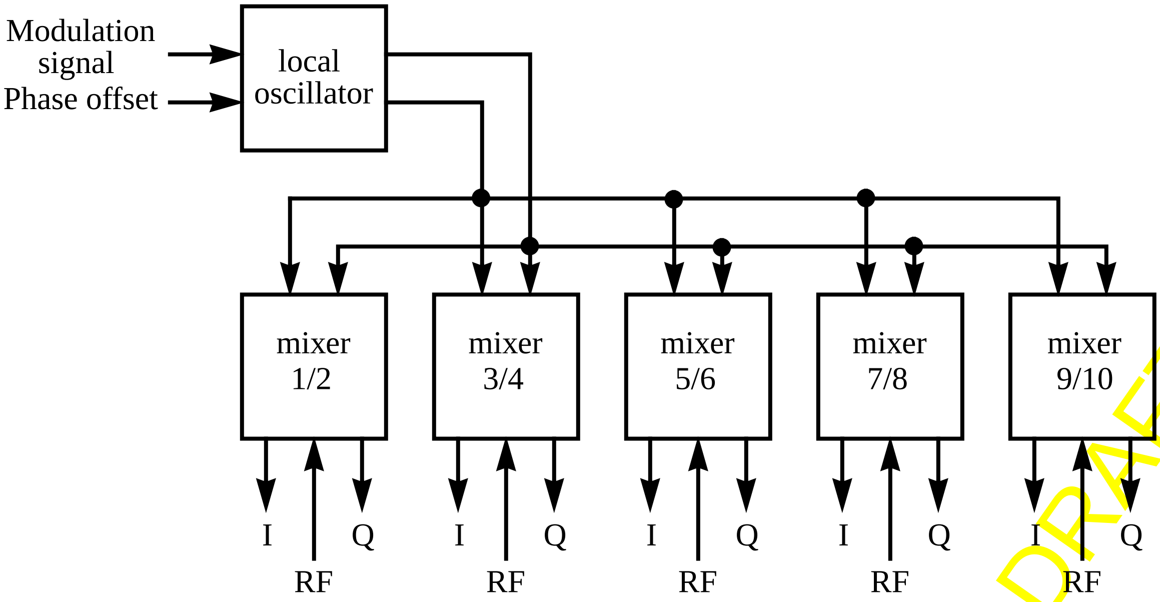

Figure 5: Demodulation (RF) part of the wavefront sensor

---

[1] Final layout made by the CDS group.

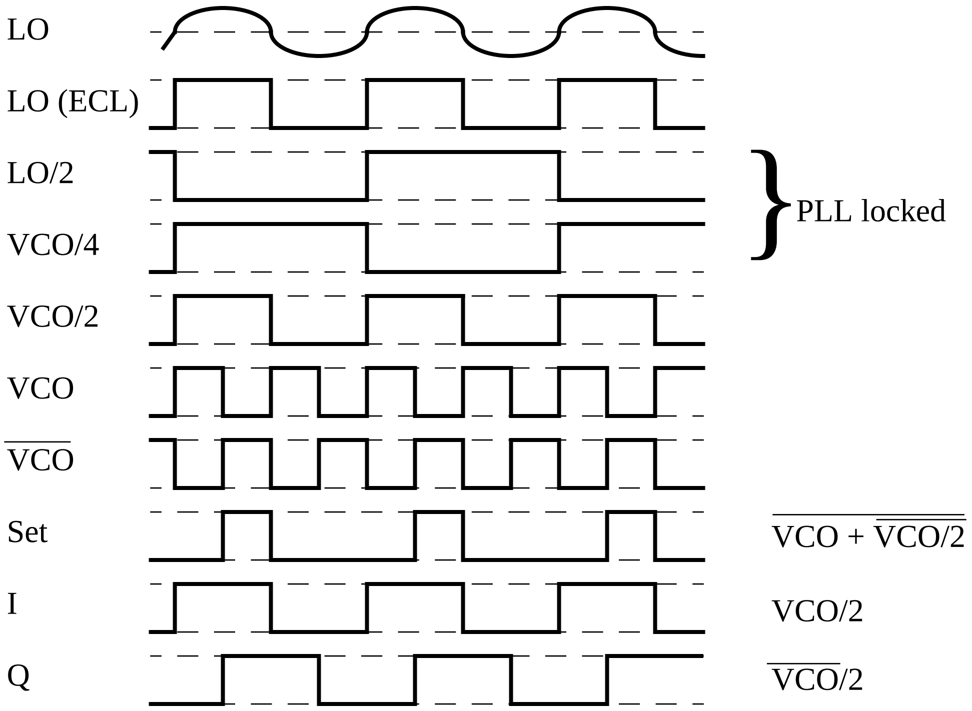

Figure 6: Timing Diagram for the PLL

3.3.2 Local Oscillator

The on-board oscillator (VCO) has to provide the required local oscillator signals for the mixers and has to have the capability to adjust its global phase over a range of at least 360°. The VCO is locked to the modulation signal with a phase locked loop (PLL); for a timing diagram see Fig. 6. The input modulation signal is converted to an ECL signal with an ultra-fast comparator (AD96687). The ECL clock signal is divided by 2 with a D-flip-flop (MC10H131), before it is fed into the phase/frequency discriminator (AD9901). This division doubles the intrinsic phase range of the phase detector to 720°, providing a good linear regime over more than 360°. The error signals of the phase/frequency discriminator is passed through a passive low pass filter with a corner frequency of 75 kHz and a lag compensation with a pole/zero pair at 0 Hz/7 kHz to the tuning input of a voltage controlled oscillator (Mini-Circuits POS-xx series, see Table 4). The parameters of the PLL compensation network are listed in Table 5. The unity gain frequency is between 30 kHz and 100 kHz depending on the type of VCO which is used.

Table 4: Recommended VCOs for different frequency ranges.

Frequency Range [MHz]	12 to 25	18 to 37	25 to 50	37 to 75	50 to 95
VCO type	POS–50	POS–75	POS–100	POS–150	POS–200

Because the output of the VCO is divided by 4 with two D-flip-flops, before it is fed into the phase/frequency discriminator, the VCO runs at double the frequency of the modulation clock signal. The in-phase (I) clock signal for the mixers is taken from the divided-by-2 signal of the VCO. The quadrature-phase (Q) clock signal is obtained by dividing the inverted VCO signal by 2 with an additional D-flip-flop. This circuit alone would have an ambiguity: either the Q signal is 90° ahead of the I signal or 90° behind. To fix this ambiguity a logical NOR operation (MC10H102) is performed from the VCO signal and the inverted divided-by-2 signal of the VCO. The resulting signal is used to either set (90° ahead) or reset (90° behind) the D-flip-flop which is responsible for the Q clock signal.

Table 5: Parameters of the PLL compensation network

Parameter	Value	Unit
Double pole	0	kHz
Low pass filter pole	75	kHz
Zero	7	kHz
Unity-gain frequency[1]	10	kHz
Phase Offset (reference input)	1.3	V/rad

1. Using the POS–50.

3.4 Control and Data Acquisition System

One wavefront sensor provides 5 (4) analog signals for the DC photocurrent and 10 (8) down-converted RF signals (I and Q phases). 5 (4) binary channels are needed to switch the additional front-end RF gain stages on and off and one analog line is needed for the phase shifter of the local oscillator (see Table 6). An addition binary indicator comes from the shutter which is used to block the incoming laser beam and one additional control line is needed to turn the calibration light source on and off. The analog input signals are digitized by a multi-channel ADC module and read into a front-end digital signal processor. For economical reasons two wavefront sensors

Table 6: Wavefront sensor signals and control lines.

Channel	No.	Type	Resolution	Bandwidth
DC photocurrent	5	analog in	16 bit	≥ 1.5 kHz
RF down-conversion	10	analog in	16 bit	≥ 1.5 kHz
LO phase shifter	1	analog out	16 bit	≥ 1.5 kHz
gain switch	5	binary out	12V o.c.	1 sec
shutter status	1	binary in	TBD	1 sec
calibration light source	1	binary out	TBD	1 sec

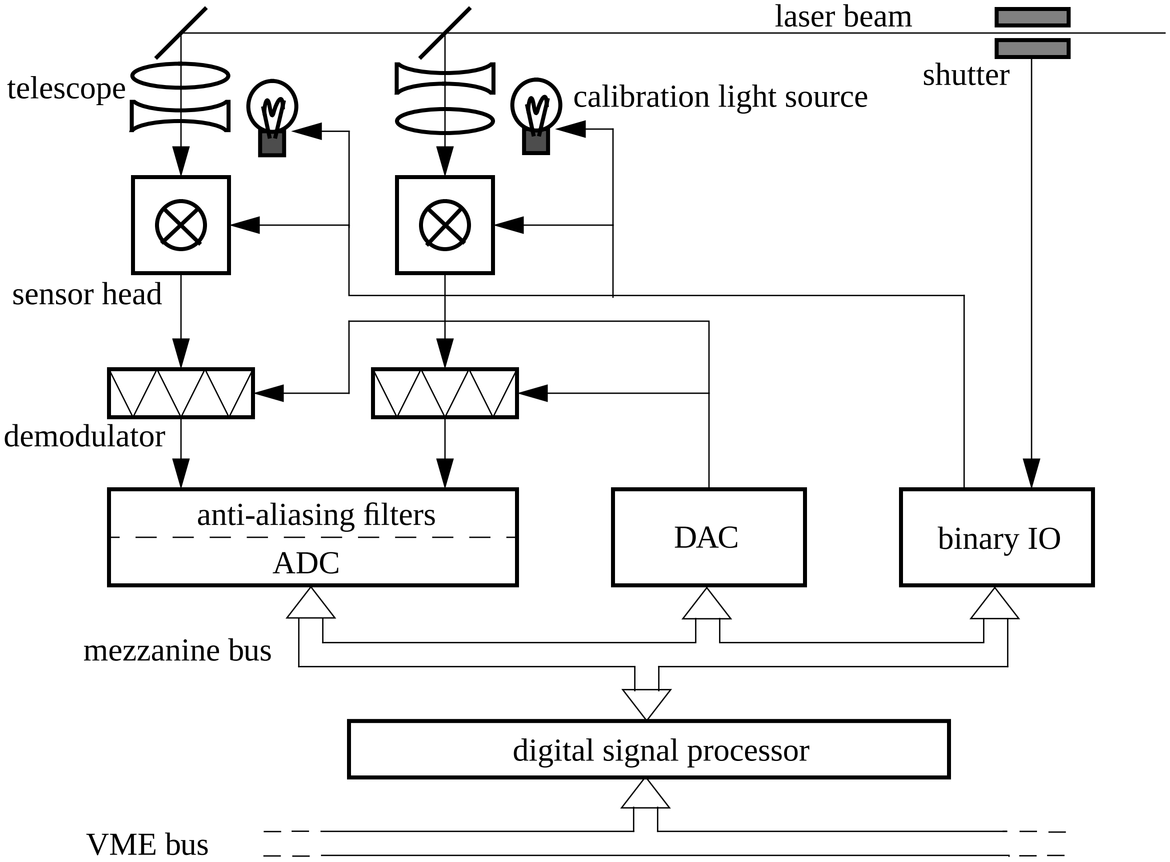

Figure 7: Hardware overview of a wavefront sensor detector unit.

are combined into one detector unit consisting of two sensor heads, two demodulator boards, a 32 channel ADC module, a 2 channel DAC module, a 16 channel binary input/output board and a digital signal processor (see Fig. 7). All these modules except the sensor heads are hosted in 19” chassis for 6U-sized boards (double europe standard) with the CPU connected to a VME bus.

The data and information flow within the digital signal processor of a wavefront sensor unit is shown in Fig. 8. The sampled data are first adjusted with the existing calibration corrections, then preprocessed and filtered. Finally, the data rate is reduced to a level suited for the alignment compensation network. Between each stage of data processing a path is provided to make high bandwidth diagnostic snapshots possible. A control record keeps track of the status of the calibration light source, the laser beam shutter, the RF gain settings, the local oscillator phase and all internal parameters. The local oscillator phase is controlled by a phase shifter routine which is able to sweep the phase through a full cycle for calibration purposes. Data which are gathered during an on-line calibration measurement can be analyzed in real-time and then used to replace the old calibration settings.

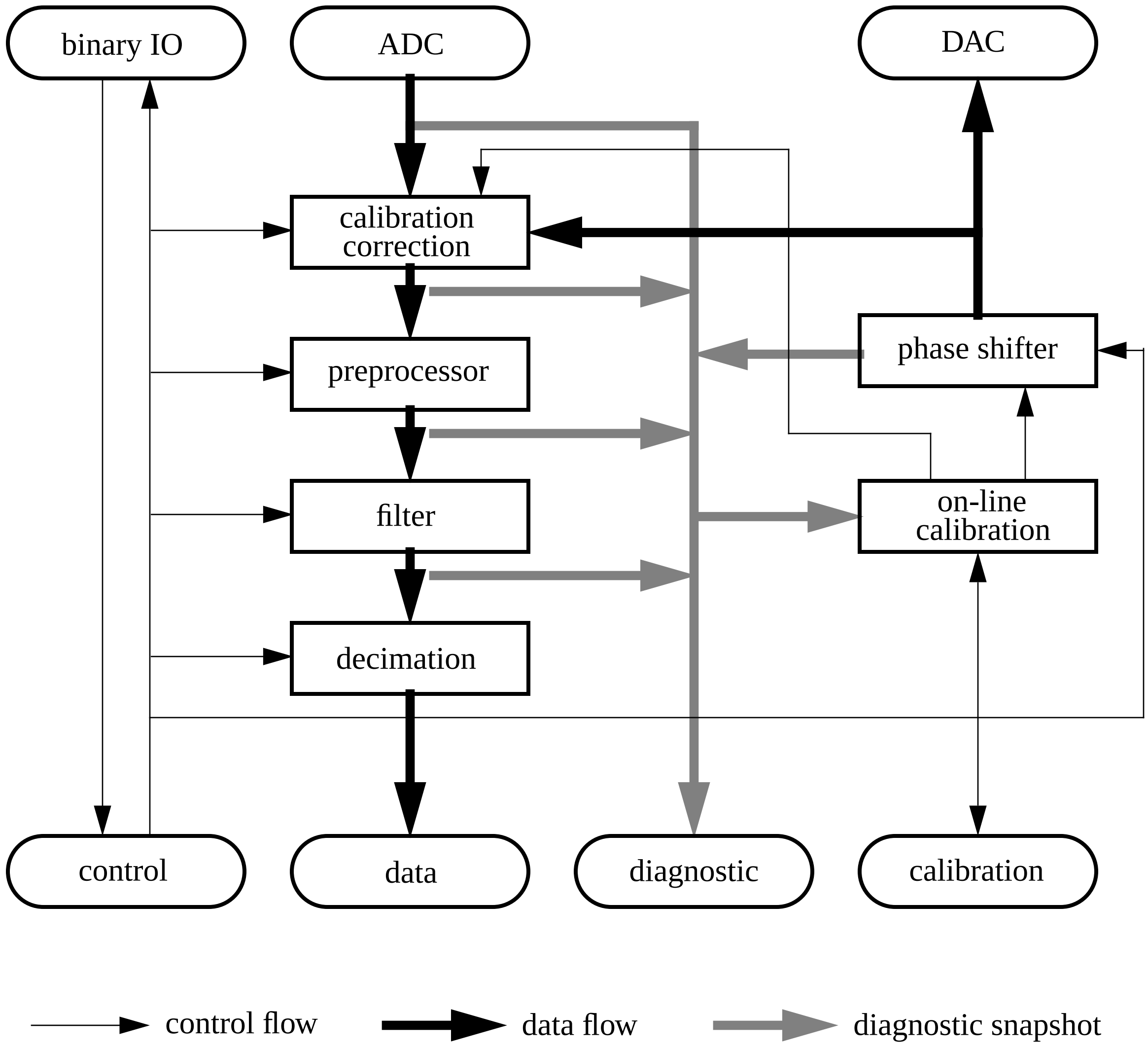

Figure 8: Data and control flow in a wavefront sensor unit.

4 CALIBRATION

4.1 Guoy Phase Calibration

TBD.

4.2 Photodiode Tuning

Each segment of the photodiode — together with the coil in parallel — forms a resonant circuit which has to be tuned to the modulation frequency. Because the capacitance of the photodiode depends only on the bias voltage, the resonance frequency must be tuned with the inductance of the coil. To suppress harmonics of the modulation frequency the capability for 2 notch filters is provided. A measurement setup is shown in Fig. 9; the corresponding calibration protocol 1 can be found in Appendix B. An RF network analyzer is used to measure the transfer function of the sensor head by sweeping the AM-modulation frequency of a laser. Because the value for the inductance of the resonant circuit depends on the notch frequencies and because the notch frequencies do not depend on the resonant circuit, the tuning of the notches has to be done first.

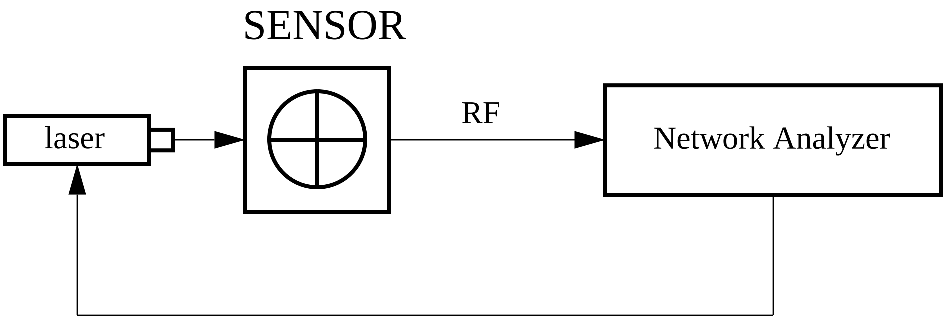

Figure 9: Setup for Photodiode Tuning.

A schematics of the tuned circuit is shown in Fig. 10. In this picture the photodiode consist of a capacitor in series with a resistor; the indicated values are consistent with both the data sheet and the measured behavior of the circuit, if the bias voltage over the photodiode is 75V. The total impedance of the tuned circuit is then given by:

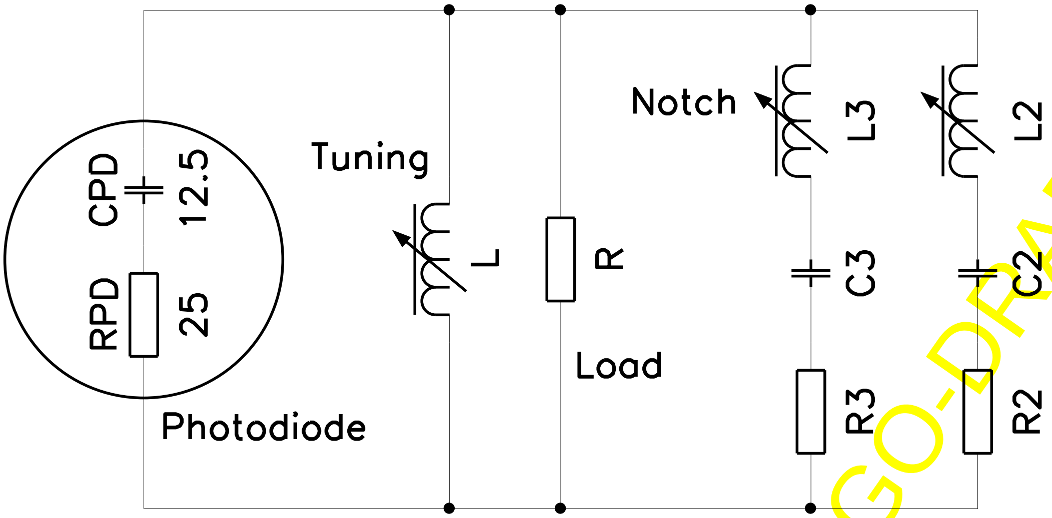

Figure 10: Schematics of the Tuned Circuit.

$$\frac{1}{Z(s)} = \frac{1}{R_{PD} + \frac{1}{sC_{PD}}} + \frac{1}{sL} + \frac{1}{R} + \frac{1}{R_2 + \frac{1}{sC_2} + sL_2} + \frac{1}{R_3 + \frac{1}{sC_3} + sL_3} \qquad (42)$$

with $s = 2\pi i f$ and $R = 24.9\ \mathrm{k}\Omega$. The notch frequencies are then given by:

$$2\pi f = \frac{1}{\sqrt{C_i L_i}} \qquad (43)$$

whereas the resonance frequency is defined as the position of the maximum impedance. To keep the inductance for the notch tuning coils at reasonable values, it is recommended to use a 10 pF capacitors in series for frequencies in the range from 20 MHz to 60MHz and to use 6.8 pF capacitors for frequencies above 60 MHz. Table 7 lists the inductance values of the tuning coils (L31-10-CT-B-4) against the number of winding turns.

Table 7: Coil Winding Data Sheet (L31-10-CT-B-4).

Turns	L (µH)	Turns	L (µH)	Turns	L (µH)
8.5	0.51	12.5	1.17	16.5	2.42
9.5	0.63	13.5	1.41	17.5	2.85
10.5	0.78	14.5	1.70	18.5	3.33
11.5	0.97	15.5	2.04	19.5	3.80

A calculated impedance transfer function is shown in Fig. 11, tuned to 25 MHz and including a notch at 50 MHz.

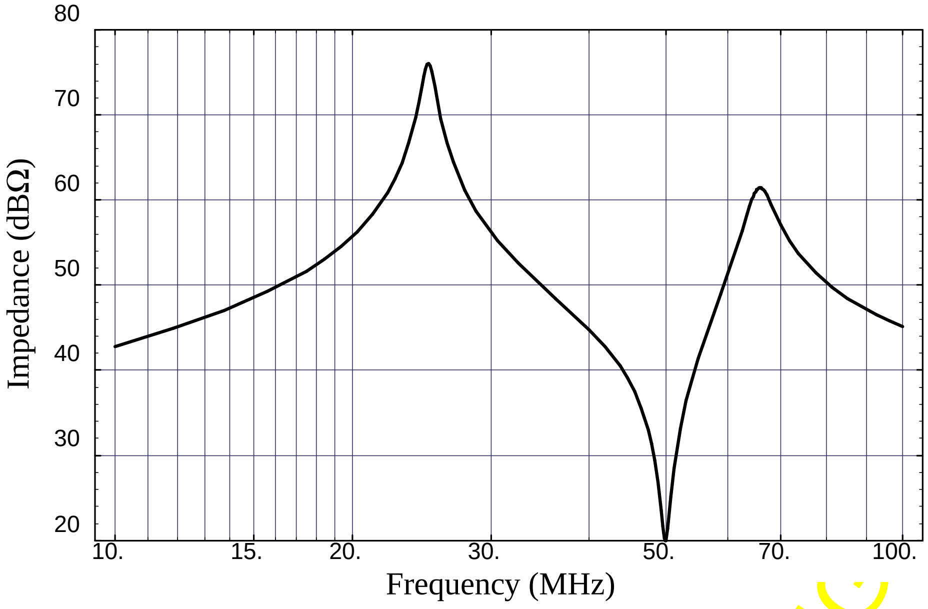

Figure 11: Calculated Impedance of the Tuned Circuit.

4.3 In-Phase and Quad-Phase Adjustment

The phase difference between the in-phase and the quad-phase can be fine-adjusted with a on-board potentiometer. A jumper can be used to select, if the quad-phase is leading or lagging relative to the in-phase. The measurement setup is shown in Fig. 12; the number of the calibration protocol is 2 and can be found in Appendix B. Two RF signal generators with a frequency offset of 1 kHz are used to drive the RF and LO inputs of the demodulator board, respectively. For each RF channel the phase difference at the 1 kHz between the in-phase and quad-phase outputs are measured with a spectrum analyzer. The average of the phase difference is then adjusted to 90° with the on-board potentiometer.

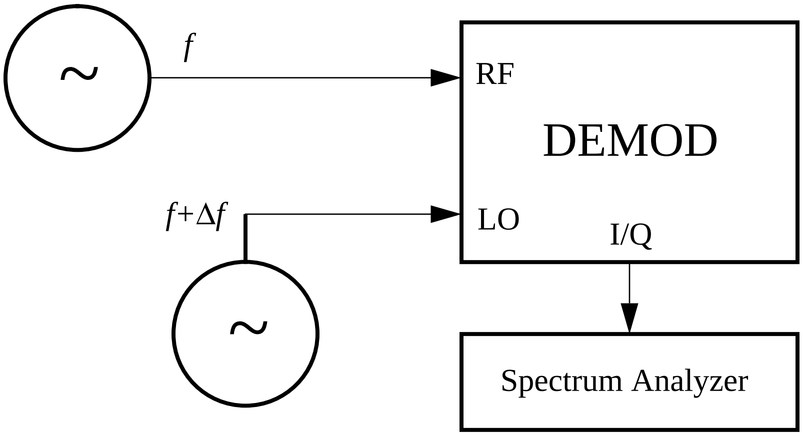

Figure 12: Setup for In-Phase and Quad-Phase Adjustment.

4.4 Offset Error Adjustment

The outputs of the solid-state mixers which are used on the demodulator board have a fairly large temperature-dependent DC offset. There are 10 potentiometers mounted on the board which are used to adjust the offset error of each mixer to zero. The measurement setup is shown in 13. The LO input of the demodulator board is connected to an RF signal generator, whereas the RF inputs are either connected to the sensor head or terminated with 50Ω resistors. It is important that the board be powered-up for a couple of hours before the offsets are adjusted, since the mixers must reach a stable temperature first. The number of the calibration protocol is 3 and can be found in Appendix B.

4.5 RF Phase Matching

Since the photodiode RF channels do not have individual phase shifters, their phases have to be adjusted by matching the cable length between the sensor head and the demodulator board (see

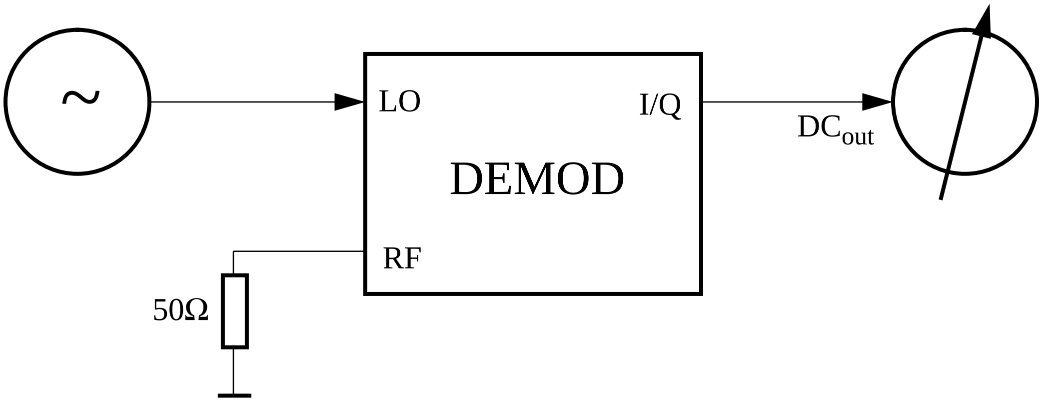

Figure 13: Setup of Offset Error Adjustment.

Appendix A.3). If the RF phases are matched within a couple of degrees, a fine adjustment can be done with the tuning circuit of the photodiode by changing the resonance frequency by a small amount. The tuning of the resonance circuit should be small enough, so that the effect on the amplitude is negligible.

The calibration setup is shown in Fig. 14. An AM-modulated laser is used to generate a synchronous RF photocurrent in each segment of the photodiode. The sensor head is connected to the demodulator board by cables of the same length. The LO input of the demodulator is driven by a frequency which has a 1 kHz offset in respect to the AM laser frequency. The RF phase is then matched by measuring the phase difference between two I channels of the demodulator board at 1 kHz and by tuning the resonance circuit coil of the second channel until the phase difference is zero. The number of the calibration protocol is 5 and can be found in Appendix B.

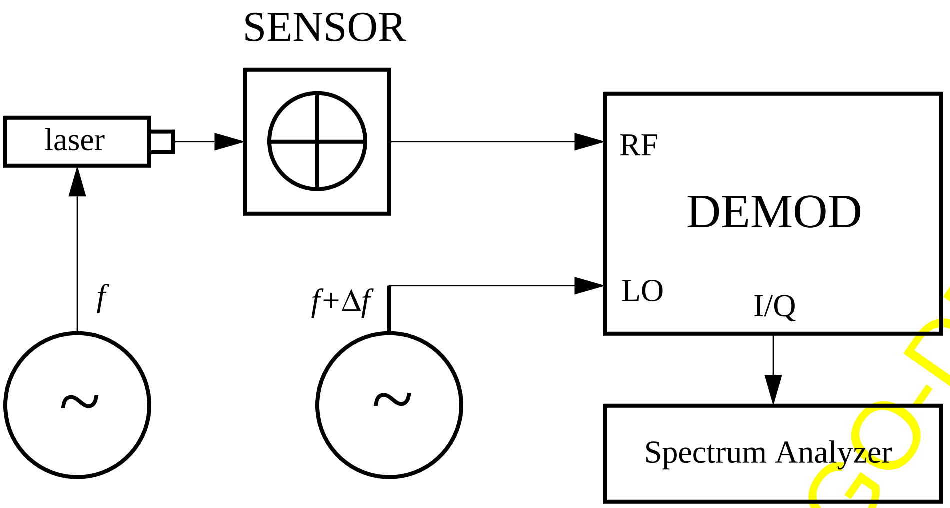

Figure 14: Setup for RF Phase Matching.

4.6 Gain Calibration

The gain of the down-conversion can be measured with the setup drawn in Fig. 15. An AM-modulated laser produces a photocurrent in the sensor head which consist of a DC and an AC component. The ratio between the two is measured with a high-bandwidth monitor photodiode. The LO input of the demodulator board is driven by an RF frequency which has a 1 kHz offset relative to the laser modulation frequency. At the output of the demodulator the r.m.s. amplitude of the down-converted 1 kHz signal can be used to calculate the RF gain of the wavefront sensor:

$$\mathrm{Gain}(\mathrm{k}\Omega) = \frac{\mathrm{AC_{out}}(\mathrm{mV})}{\mathrm{DC_{out}}(\mu\mathrm{A}) \times \mathrm{Modulation\ Depth}(\mathrm{I_{AC}}/\mathrm{I_{DC}})} \tag{44}$$

To obtain the voltage-to-light-power gain one has to multiply the above number with the efficiency of the photodetector which is usually given in Watts/Ampere. The number of the corresponding calibration protocol is 5 and can be found in Appendix B.

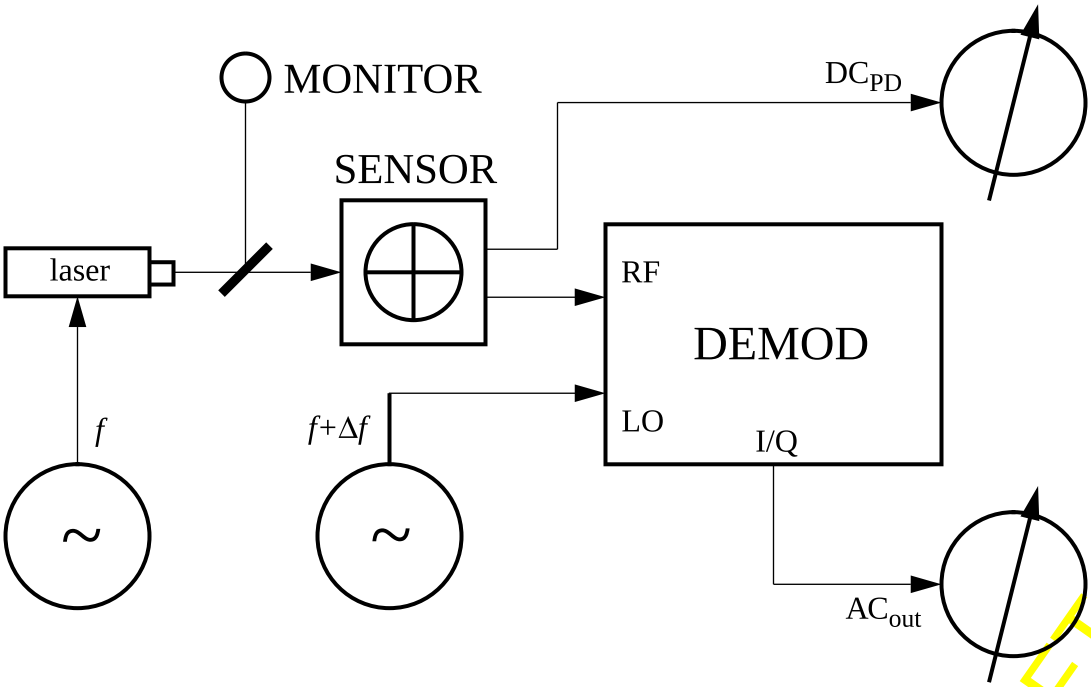

Figure 15: Setup for Gain Calibration.

4.7 Phase Shifter Calibration

The conversion factor of the phase shifter is calibrated with the setup drawn out in Fig. 16 using calibration protocol 6. The RF and LO input of the demodulator board are connected to the same RF frequency generator which provides a 10 dBm sine wave for each channel. The phase reference input of the demodulator board is controlled by a DC source which can be adjusted between –10V and +10V. First, this voltage ($\mathrm{DC_{in}}$) is turned down from zero until the output voltage (DC_{out}) is exactly zero. Then, it is turned up until an other zero crossing is reached. This voltage change corresponds to a phase shift of 180°.

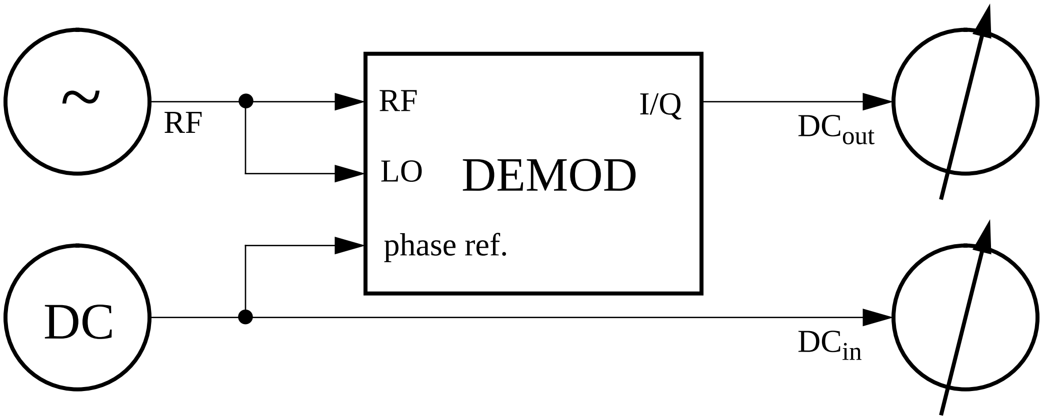

Figure 16: Phase Shifter Calibration Setup.

4.8 Shot Noise Measurements

The shot noise measurement has to be done with a light source which has a white noise spectrum, e.g. a light bulb (see Fig. 17). The DC photocurrent I_{PD} is used to calculate the shot noise level:

$$\text{shot noise} = \sqrt{2QI_{PD}} \tag{45}$$

where Q is the elementary charge.

The down-converted noise level S is the square root of the quadratic sum of shot noise and the electronic noise N which can be measured during darkness, i.e. the light bulb has to be switched off. The corresponding calibration protocol 7 can be found in Appendix B. The RF gain is then obtained by:

$$\text{Gain} = \sqrt{\frac{S^2 - N^2}{4QV_{\mathrm{DC}}/R_{\mathrm{DC}}}} \tag{46}$$

where $V_{\mathrm{DC}}/R_{\mathrm{DC}}$ is the DC photocurrent. The RF gain of the sensor head is given in Ω, when S and N are measured in $V/\sqrt{\mathrm{Hz}}$. Clearly, for a high precision gain calibration through a shot noise measurement the shot noise has to be much larger than the intrinsic electronic noise. This condition is only fulfilled at a rather large photocurrent, since the shot noise starts to dominate above about 50 µA photocurrent. By connecting an RF spectrum analyzer directly to the RF output of the sensor head the gain of the sensor head can be measured independently.

If the light power per unit area is measured with a power meter, the efficiency of the photodetector can be deduced from the measurement of the DC photocurrent and the size of the detector segment.

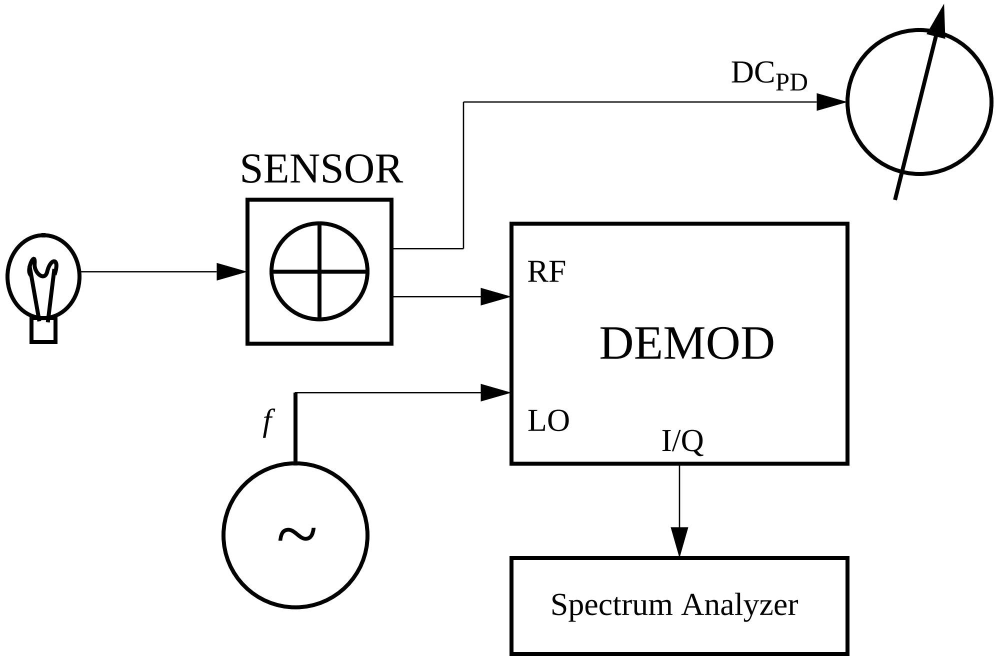

Figure 17: Setup for Shot Noise Measurement.

4.9 Common Mode Rejection Ratio

The common mode rejection is a combination of the uniformity of the photodiode response, the electronic gain and the corrections which might be applied to the measured signals. Since the DC and RF gain stages are different, the common mode rejection ratio for DC and RF signals might not be the same. Hence, the difference in response to a uniform light source has to be measured for both the DC and the RF part separately. A uniform light source can be produced by placing the light bulb of the shot noise measurement (see Fig. 17) far enough away from the sensor head, so that each photodiode segment sees the light source at the same distance. Since the shot noise measurements already measured the DC gains of each channel, they can be directly used to correct the RF/DC measurements done with the AM-modulated laser. This allows to determine the RF gain for each channel and, therefore, the common mode rejection ratio between the RF channels. The difference in the DC response between opposite photodiode segments has be taken into account when the photodetector is centered to the incident laser beam coming from the interferometer. The differences in the RF response between individual channels can be corrected for in software after the signals are digitized, in order to improve the common mode rejection ratio. This should guarantee a common mode rejection ratio of at least 30 dB.

5 SIGNAL PROCESSING

5.1 Signal Conditioning

The first step of the signal processing are the adjustments due to the electronic gain and the DC offset errors which were measured during the calibration procedure:

$$S_{\text{corr.}} = R_{\text{gain}}(S_{\text{meas.}} - S_{\text{DC offset}}) \tag{47}$$

where $S_{\text{meas.}}$ is the measured ADC value, $S_{\text{DC offset}}$ is the measure DC offset error and R_{gain} the measured gain. The resulting quantity $S_{\text{corr.}}$ is then a direct measure of the photocurrent in physical units. The next step is the selection of the phase of the demodulation frequency. If one uses the notation I and Q for the signal in the ‘in-phase’ and the ‘quad-phase’, respectively, one can write the measured signal as a complex number with the I and Q signal as the real and imaginary part, respectively,

$$S_{\text{corr.}} = S^I_{\text{corr.}} e^{i\frac{\Delta\phi^d_{LO}}{2}} + iS^Q_{\text{corr.}} e^{-i\frac{\Delta\phi^d_{LO}}{2}} \tag{48}$$

where $\Delta\phi^d_{LO}$ is the deviation of the phase difference of the two I and Q mixers from 90°. The amplitude A_0 of an RF signal with phase ϕ_0 can be obtained from the real part of the above signal phase shifted by the difference between the local oscillator phase ϕ_{LO} and the RF phase

$$A_0 = \text{Re}(S_{\text{corr.}} e^{i(\phi_{LO} - \phi_0)}) \tag{49}$$

By adjusting the local oscillator phase, so that $\phi_{LO} = \phi_0$, the interesting RF signal is contained in the I phase only and no phase shifting in software has to be performed.

5.2 On-line Calibration

From the previous section one sees that one needs to have calibration values for the DC offset error the electronic gain, the local oscillator phase and the difference in phase between the I and Q phase mixer. Since the dependence of the signal A_0 from the local oscillator phase error $\Delta\phi^c_{LO}$ and from the phase difference error $\Delta\phi^d_{LO}$ is of second order, only the DC offset error and the electronic gain have to be calibrated periodically during operation. The measurement of the DC offset is done by blocking all the light to the photodiode, whereas the gain determination is done by measuring the shot noise induced RF signal, when the calibration light source is turned on.

In a null servo system DC offsets in the error signals are usually more harmful than gain errors, because the servo has to adjust the entire system to cancel the offset errors, whereas a gain error only affects the bandwidth of the servo and as a consequence might change the phase margin slightly. Unfortunately, the DC offset at the output of the Gilbert-cell mixers used on the demodulator boards are rather large and temperature dependent. Therefore, they have to be closely watched during operation.

One way to get rid of the DC offset errors of the mixers is to apply a phase modulation $\phi(t)$ to the local oscillator signal with a frequency a few times greater than the servo bandwidth. The true DC signal then gets up-converted and stays unaffected from the DC offset errors. The final down-conversion for obtaining the original DC signal is done only after the digitalization in software. If one writes the RF signal as $A_0 e^{i\phi_0}$, the phase of the local oscillator as the sum of the indented phase and its error $\phi_{LO}(t) = \phi(t) + \Delta\phi(t)$, the converted signal becomes

$$S = \{A_0 e^{i\phi_0} e^{-i(\phi(t) - \Delta\phi(t))} + A_{\mathrm{DC\ offset}}\} e^{i(\phi(t) - \phi_0)} = A_0 e^{i\Delta\phi(t)} + A_{\mathrm{DC\ offset}} e^{i(\phi(t) - \phi_0)} \qquad (50)$$

Feeding the signal through an additional digital low-pass filter which has corner frequency below the local oscillator phase modulation frequency will remove any remaining part of the up-converted DC offset error and will at the same time remove any time dependent part of the phase error $\Delta\phi(t)$.

5.3 Data Reduction

From the 15 signals which are sampled at high speed for each wavefront sensor only two physical meaningful misalignment angles can be deduced. Since the bandwidth of the angular servo is rather low (1 Hz to 10 Hz), the data also have to be filtered and decimated. The data flow in the front-end processor is shown in Fig. 8. In the first step a horizontal and vertical misalignment angle is calculated from the digitized and conditioned data (see the two previous sections) by subtracting the signals from opposite photodiode segments and by applying a voluntary correction for the centering error of the laser beam on the photodiode (see section 2.2.1.3). The next step uses a digital low-pass filter to reduce the bandwidth of the sampled data to about ten times the servo bandwidth. In the last step the data are decimated, so that their rate is not much higher than twice the filter bandwidth.

APPENDIX A INTEGRATION

A.1 Sensor Head Enclosure

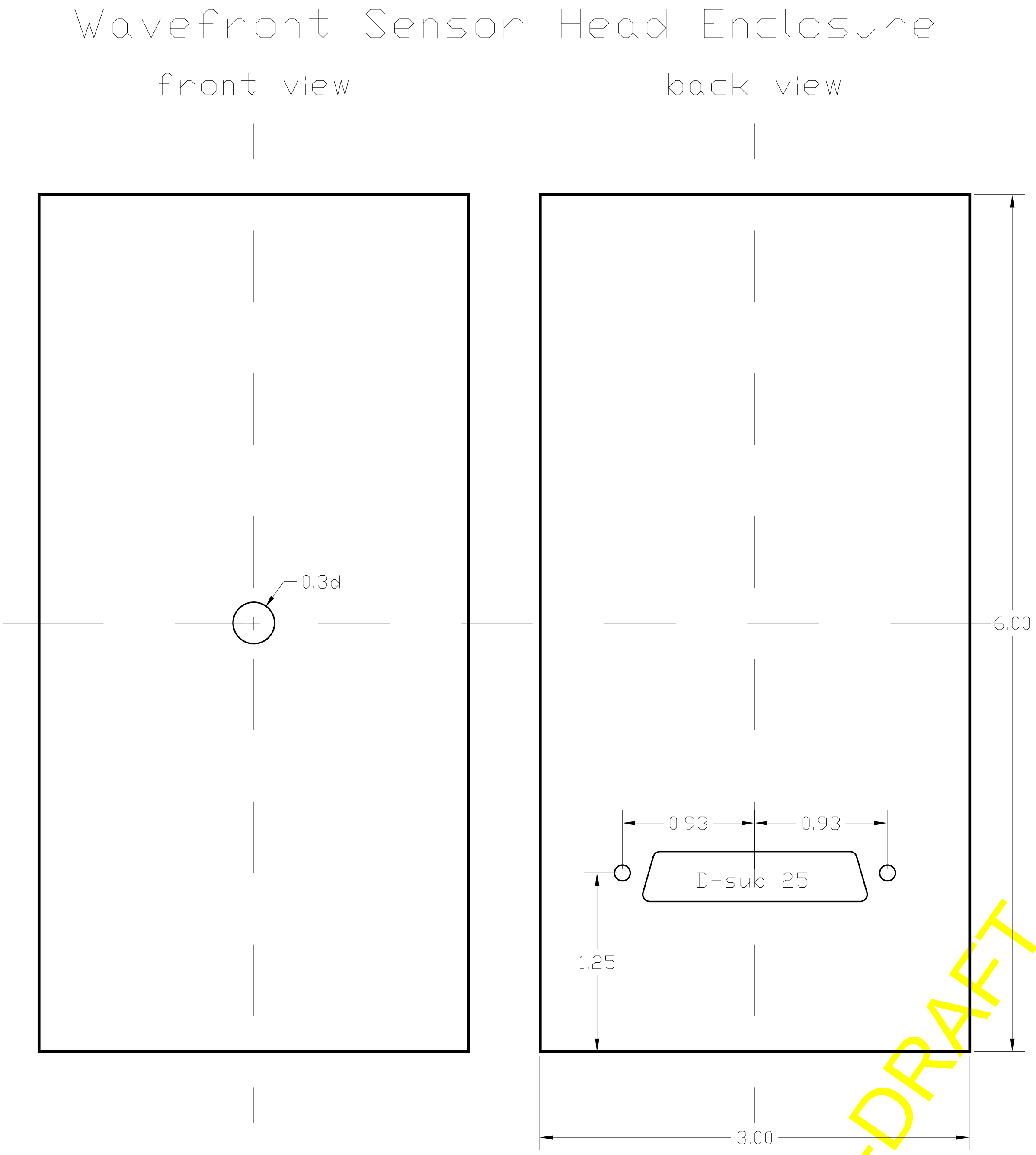

0.3 diameter hole is a thru hole
D-sub 25 is an open hole for a 25 pin D-sub socket
Units are in inch; all tolerances are +/- 0.005

Figure 18: Wavefront sensor head: Enclosure front and back view

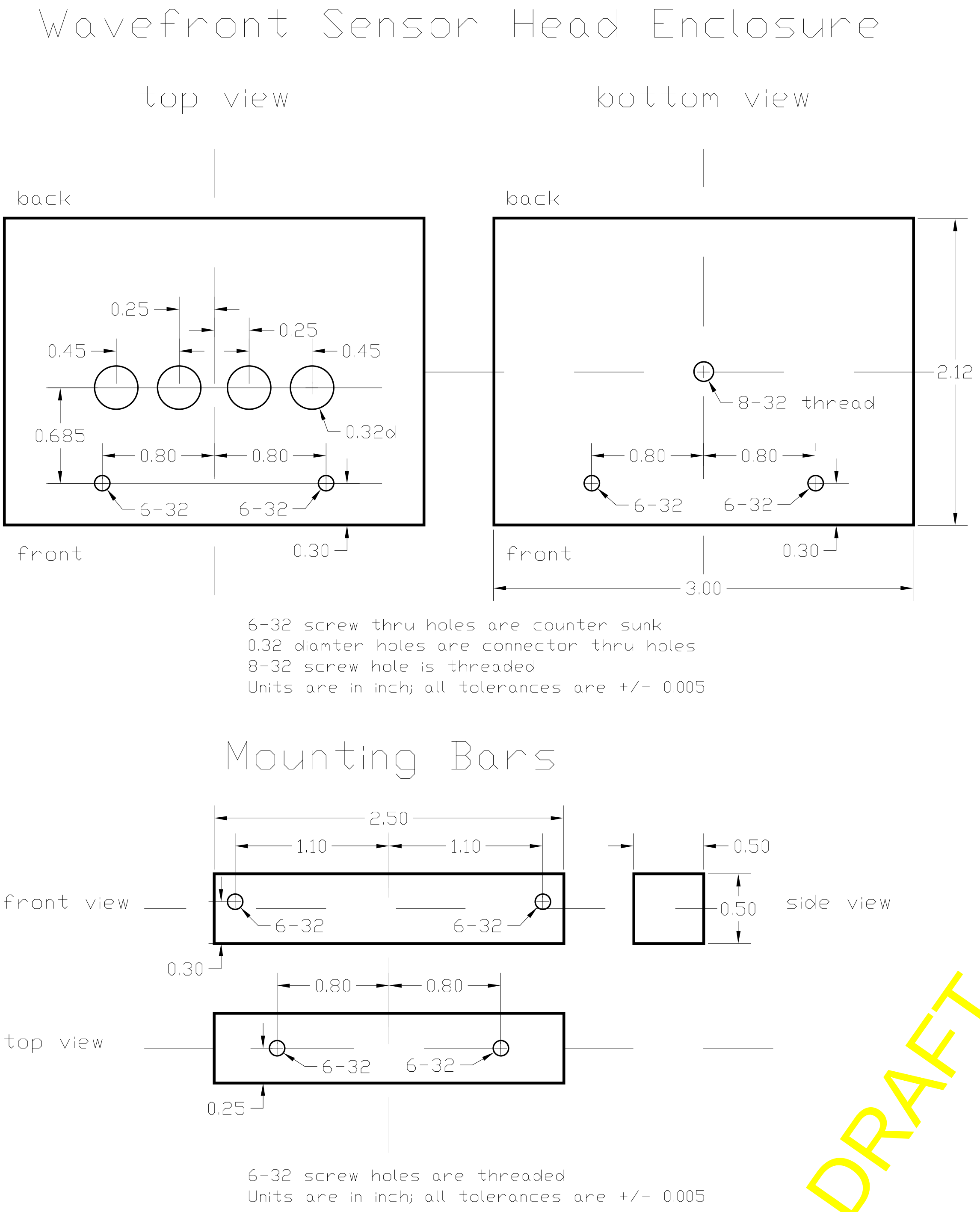

Figure 19: Wavefront sensor head: Enclosure top and bottom view

A.2 Connector Pin-Outs

Table 8: Pin Assignment

Pin	JK1	JK2	P2, Row C
1	DC 1 +	DC 1 +	GND
2	DC 2 +	DC 2 +	GND
3	DC 3 +	DC 3 +	+5.2V
4	DC 4 +	DC 4 +	+5.2V
5	DC 5 +	DC 5 +	+5.2V
6	JK2-16 / Gain 1	I 1 +	+5.2V
7	JK2-17 / Gain 2	I 2 +	GND
8	JK2-18 / Gain 3	I 3 +	GND
9	JK2-19 / Gain 4	I 4 +	–5.2V
10	+12V	I 5 +	–5.2V
11	–12V	Q 1 +	–5.2V
12	Bias Voltage	Q 2 +	–5.2V
13	n.c.	Q 3 +	GND
14	DC 1 –	Q 4 +	GND
15	DC 2 –	Q 5 +	+24V
16	DC 3 –	JK1-6	+24V
17	DC 4 –	JK1-7	GND
18	DC 5 –	JK1-8	GND
19	JK2-35 / Gain GND	JK1-9	–24V
20	JK2-36 / Gain GND	DC 1 –	–24V
21	JK2-37 / Gain GND	DC 2 –	GND
22	Gain GND	DC 3 –	GND
23	GND	DC 4 –	n.c.
24	GND	DC 5 –	n.c.
25	GND	I 1 –	n.c.
26		I 2 –	n.c.
27		I 3 –	n.c.
28		I 4 –	n.c.
29		I 5 –	n.c.
30		Q 1 –	Bias Voltage
31		Q 2 –	n.c.
32		Q 3 –	n.c.
33		Q 4 –	
34		Q 5 –	
35		JK1-19	
36		JK1-20	
37		JK1-21	

Table 9: List of Connectors

Designator	Location	Type	Signals
J1 to J5	front / demodulator top / sensor head	LEMO coax	Preamplified RF Signal 1 to 5
J6 / J7	front / demodulator	LEMO coax	Local oscillator signal / phase reference
J8 / J9	front / demodulator	LEMO coax	In-phase and quad-phase clock
JK1	front / demodulator rear / sensor head	D-sub 25 pin	Photodiode DC signals and power supply for sensor head
JK2	front / demodulator	D-sub 37 pin	Output signals: down-converted and DC
P1	rear / demodulator	DIN C	n.c.
P2	rear / demodulator	DIN C	Power supply on row C, row A and B n.c.

A.3 Cable Specifications

The RF cables between the wavefront sensor head and the demodulator have to be phase-matched, since the RF-phases between individual channels are not adjustable otherwise. Therefore, the cable length (signal delay) within one set of five coaxial cables must be the same with a precision of 10 mm (0.5 ns). The connectors on both ends are coaxial LEMO plugs from the NIM-CAMAC 00-series. The cables within one set should be labeled from 1 to 5, since the fine-adjustment of the RF phases are made with the tuning circuits of the sensor head.

A.4 Manufacturing Instructions

A.4.1 Sensor Head

- Make the following modification to the board: (a) remove the short trace segment between R23 and R30 on the top, (b) stand R23 and C44 on end on the inside pad at the R23 site, and solder them together in parallel; one end of each is on the board, the other end sticking up and (c) solder a short wire between the top end of the R23/C44 to R30.
- Solder all components except the photodiode U1, the coils L2 to L13, the capacitors C23 to C26, C30, C43, C56 and C69 and the resistors R1 to R4. (Be sure to use high-voltage capacitors for C21 and C22.)
- Add four additional 10 pF capacitors parallel to (on top of) R2, R28, R44 and R60.
- Mount board into enclosure and make the flat ribbon cable (DB25/IDC26) connecting them.
- Solder the photodiode U1 on the board, make the tuning coils and tune the circuit.

A.4.2 Demodulator Board

TBD.

A.5 Bill of Materials

A.5.1 Sensor Head

Table 10: Bill of Materials for the Sensor Head.

Qty.	Component	Value	Refs
1	SD225-23-21-040		U1
4	1N4148		CR1 CR2 CR3 CR4
2	7805/7905		VR1 VR2
4	9202-12-00		RY1 RY2 RY3 RY4
4	AD827		U10 U11 U12 U13
8	CLC425		U2 U3 U4 U5 U6 U7 U8 U9
1	inductor	8.2 µH	L1
12	L31-10-CT-B-4		L2 L3 L4 L5 L6 L8 L10 L12 L7 L9 L11 L13
4	capacitor	1 nF	C29 C42 C55 C68
4	capacitor	2.2 nF	C32 C45 C58 C71
14	capacitor	10 nF	C21 C22 C27 C28 C31 C40 C41 C44 C53 C54 C57 C66 C67 C70
28	capacitor	100 nF	C33 C34 C35 C36 C37 C38 C39 C46 C47 C48 C49 C50 C51 C52 C59 C60 C61 C62 C63 C64 C65 C72 C73 C74 C75 C76 C77 C78
4	capacitor	10 pF	
8	capacitor	vary	C30 C43 C56 C69 C23 C24 C25 C26
2	tant. cap.	100 nF	C19 C20
2	tant. cap.	330 nF	C9 C10
16	tant. cap.	3.3 µF	C1 C2 C3 C4 C5 C6 C7 C8 C11 C12 C13 C14 C15 C16 C17 C18
8	resistor	1.00 k	R11 R13 R27 R29 R43 R45 R59 R61
4	resistor	1.50 k	R10 R26 R42 R58
8	resistor	100	R8 R18 R24 R34 R40 R50 R56 R66
8	resistor	1.33 k	R14 R20 R30 R36 R46 R52 R62 R68
4	resistor	182	R15 R31 R47 R63
4	resistor	1 M	R1 R2 R3 R4
4	resistor	20.0	R17 R33 R49 R65
8	resistor	24.9 k	R6 R7 R22 R23 R38 R39 R54 R55
8	resistor	3.32 k	R5 R9 R21 R25 R37 R41 R53 R57
4	resistor	301	R16 R32 R48 R64
4	resistor	50.0	R19 R35 R51 R67
4	resistor	6.04	R12 R28 R44 R60
1	IDC26		J5
1	DB25		
4	LEMO coaxial		J6 J7 J8 J9
192	total		

A.5.2 Demodulator Board

Table 11: Bill of Materials for the demodulator board.

Qty.	Component	Value	Refs
1	switch	7101	SW1
10	pot.	50k	R1, R4, R7, R10, R13, R65, R68, R71, R74, R77
1	pot.	10k	R43
1	pot.	5k	R44
11	resistor	46.4k	R2, R5, R8, R11, R14, R66, R69, R72, R75, R78, R96
1	resistor	39k	R49
30	resistor	4.87k	R16, R18, R19, R21, R22, R33, R34, R36, R42, R46, R48, R52, R54, R55, R57, R58, R62, R68, R64, R80, R82, R83, R94, R97, R99, R108, R111, R113, R115
4	resistor	4.75k	R101, R103, R110, R114
10	resistor	2.87k	R17, R20, R35, R45, R53, R56, R63, R81, R98, R112
10	resistor	2k	R37, R42, R103, R107
1	resistor	887	R100
4	resistor	887	R130, R131, R134, R141
18	resistor	511	
10	resistor	402	R24, R26, R28, R30, R32, R85, R87, R89, R91, R93
2	resistor	182	R136, R137
4	resistor	130	R51, R59, R124, R139?
4	resistor	80.6	R50?, R60?, R122?, R138?
20	resistor	51.1	R23, R25, R27, R29, R32, R84?, R86?, R88?, R90, R92, R95, R100?, R117?, R194?, R???, R???, R???
1	resistor	47.5	R142?
3	jumper		JP1-JP3
1	LM7915	–15V	U5
1	LM7912	–12V	U2
1	LM7815	+15V	U4
1	LM7812	+12V	U1
6	AD OP284		U3, U12, U18, U19, U27, U29
1	AD9901		U37
1	AD96687		U28
10	AD831		U13-U17, U30-U34
10	AD797		U6-U10, U21-U25
1	AD588		U11
2	10H131	ECL	U26, U36
1	10H102	ECL	U35
2	DIN C96	male	P1, P2
1	DB37	female	J6
1	DB25	female	J7
2	LEMO EPY	coax	J8-J9

Table 11: Bill of Materials for the demodulator board.

Qty.	Component	Value	Refs
5	LEMO	coax	J1-J5
10	capacitor	1 nF	C43, C49, C55, C61, C67, C142, C148, C154, C160, C166
20	capacitor	33 nF	C4o, C42, C46, C48, C52, C54, C58, C60, C64, C66, C139, C141, C145, C147, C151, C153, C157, C159, C163, C165
2	capacitor	11 pF	C181, C215
10	capacitor	6.8 pF	C31-C35, C127-C131
10	capacitor	100 µF	C1, C2, C5, C8-C10, C16, C21, C29, C30
20	capacitor	3.3 µF	C16, C27, C36-C38, C71, C73, C74, C77, C79, C111-C113, C125, C132, C133, C136, C170, C174, C175
9	capacitor	100 nF	C3, C4, C6, C7, C19, C20, C76, C177, C179
135	capacitor	10 nF	C11-C15, C17, C22-C26, C28, C39, C41, C44, C45, C47, C50, C51, C53, C56, C57, C59, C62, C63, C65, C68-C70, C72, C75, C78, C80-C110, C114-C124, C126, C134, C135, C137, C138, C140, C143, C144, C146, C149, C150, C152, C155, C156, C158, C161, C162, C164, C167-C169, C171-C173, C176, C178, C180, C182-C214, C216
1	D96-0025-00-C		printed wiring board

APPENDIX B CALIBRATION PROTOCOLS

Table 12 lists the necessary test equipment to perform the calibration of the wavefront sensors. There is a separate calibration protocol for each calibration step added to the Appendix. A detailed description of the calibration procedure can be found in Chapter 4 on page 26.

Table 12: Necessary Test Equipment for Calibration Procedure.

	Guoy phase calibration	Photodiode tuning	In- and quad-phase adjustment	Offset error adjustment	RF phase matching	Gain calibration	Phase shifter calibration	Shot noise measurements	Common mode rejection ratio
AM-modulated laser source (10 to 100 MHz)		✔			✔	✔			
Light bulb (white noise source)								✔	✔
RF signal generator 1 (10 to 100 MHz)			✔	✔	✔	✔	✔		
RF signal generator 2 (10 to 100 MHz)			✔		✔	✔			
Wideband monolithic photodiode (up to 100 MHz)						✔			
DC voltage source (max. 10V)							✔		
RF network analyzer (up to 100 MHz)		✔							
RF spectrum analyzer (up to 100 MHz)								✘	
Spectrum analyzer (0 to 10 kHz)			✔		✔			✔	✔
DC voltmeter (max. 10V)				✔		✔	✔	✔	✔
AC voltmeter (max. 10V)						✔			
Scope (up to 100 MHz)		✘	✘		✘	✘	✘		

✔ necessary; ✘ optional.

WFS CALIBRATION PROTOCOL 1	Date: Time:	Serial number:
Photodiode Tuning	Signature:	

Channel	Photodiode current (μA)	Coil (turns) / Capacitor (pF)			Tuning frequencies (MHz)		
		Notch 1	Notch 2	Resonance	Notch 1	Notch 2	Resonance
1		L	L	L	*f*	*f*	*f*
		C	C		Γ	Γ	Γ
					gain (dB)	gain (dB)	gain (dB)
2		L	L	L	*f*	*f*	*f*
		C	C		Γ	Γ	Γ
					gain (dB)	gain (dB)	gain (dB)
3		L	L	L	*f*	*f*	*f*
		C	C		Γ	Γ	Γ
					gain (dB)	gain (dB)	gain (dB)
4		L	L	L	*f*	*f*	*f*
		C	C		Γ	Γ	Γ
					gain (dB)	gain (dB)	gain (dB)
5		L	L	L	*f*	*f*	*f*
		C	C		Γ	Γ	Γ
					gain (dB)	gain (dB)	gain (dB)

Add a plot of the transfer function for each channel.

BIAS voltage = V

WFS CALIBRATION PROTOCOL 2	Date: Time:	Serial number:
In-Phase and Quad-Phase Adjustment	Signature:	

Channel	Frequency		Quad-Phase (lead/lag)	Phase Difference (°)	
	LO (MHz)	RF Offset (Hz)		before	after
1		+1000			
2		+1000			
3		+1000			
4		+1000			
5		+1000			
Average					

WFS CALIBRATION PROTOCOL 3	Date: Time:	Serial number:
Offset Error Adjustment	Signature:	

Channel	LO frequency (MHz)	In-Phase DC Offset (mV)	Quad-Phase DC Offset (mV)
1			
2			
3			
4			
5			

WFS CALIBRATION PROTOCOL 4	Date: Time:	Serial number:
RF Phase Matching	Signature:	

Channels		Frequency		Coil detuning (turns)	Phase difference (°)	
First	Second	LO (MHz)	RF Offset (Hz)		before	after
3	1		+1000			
3	2		+1000			
3	4		+1000			
3	5		+1000			

WFS CALIBRATION PROTOCOL 5	Date: Time:	Serial number:
Gain Calibration	Signature:	

Channel	Frequency		Photodiode current (μA)	Modulation (I_{AC}/I_{DC})	Low gain setting (I/Q)				High gain setting (I/Q)			
	LO (MHz)	Offset (Hz)			V_{AC}^{out} (mV)		Gain (kΩ)		V_{AC}^{out} (mV)		Gain (MΩ)	
1		+1000										
2		+1000										
3		+1000										
4		+1000										
5		+1000										

WFS CALIBRATION PROTOCOL 6	Date: Time:	Serial number:
Phase Shifter Calibration	Signature:	

Channel	Frequency LO (MHz)	DC_{in}^{low} (V)		DC_{in}^{med} (V)		DC_{in}^{high} (V)		$DC_{in}^{high} - DC_{in}^{low}$ (V)	
		I-phase	Q-phase	I-phase	Q-phase	I-phase	Q-phase	I-phase	Q-phase
1									
2									
3									
4									
5									
							Average		

⇒ mV/°

WFS CALIBRATION PROTOCOL 7	Date: Time:	Serial number:
Shot Noise Measurements	Signature:	

Channel	DC_{out} (V)	Low gain setting (I/Q)						High gain setting (I/Q)					
		$N\,(\mu V/\sqrt{Hz})$		$S\,(\mu V/\sqrt{Hz})$		Gain (kΩ)		$N\,(\mu V/\sqrt{Hz})$		$S\,(\mu V/\sqrt{Hz})$		Gain (MΩ)	
1													
2													
3													
4													
5													

APPENDIX C SCHEMATICS AND LAYOUT

C.1 Sensor Head

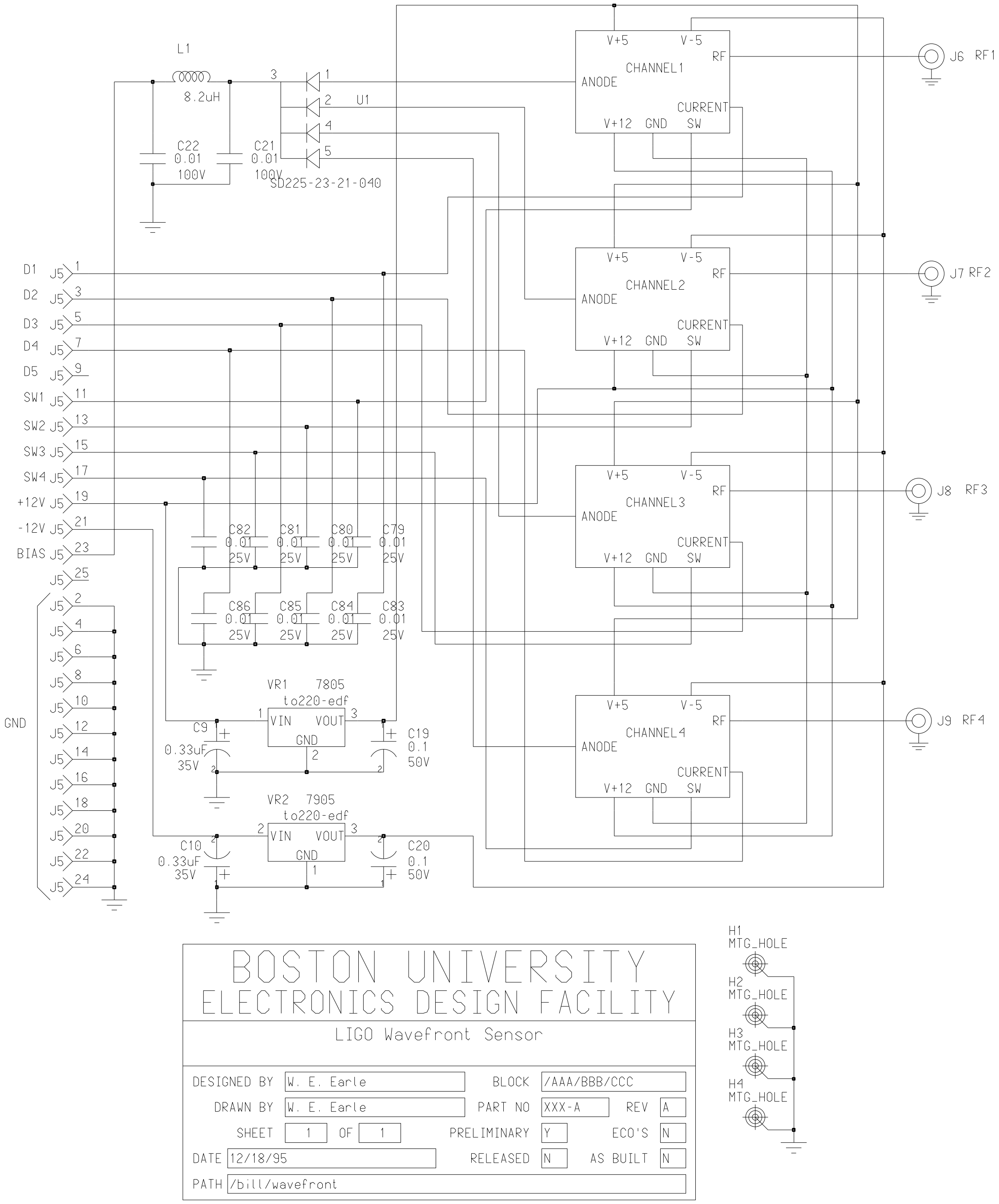

BOSTON UNIVERSITY
ELECTRONICS DESIGN FACILITY

LIGO Wavefront Sensor

DESIGNED BY W. E. Earle
BLOCK /AAA/BBB/CCC
DRAWN BY W. E. Earle
PART NO XXX-A
REV A
SHEET 1 OF 1
PRELIMINARY Y
ECO'S N
DATE 12/18/95
RELEASED N
AS BUILT N
PATH /bill/wavefront

Figure 20: Wavefront sensor head: Overview

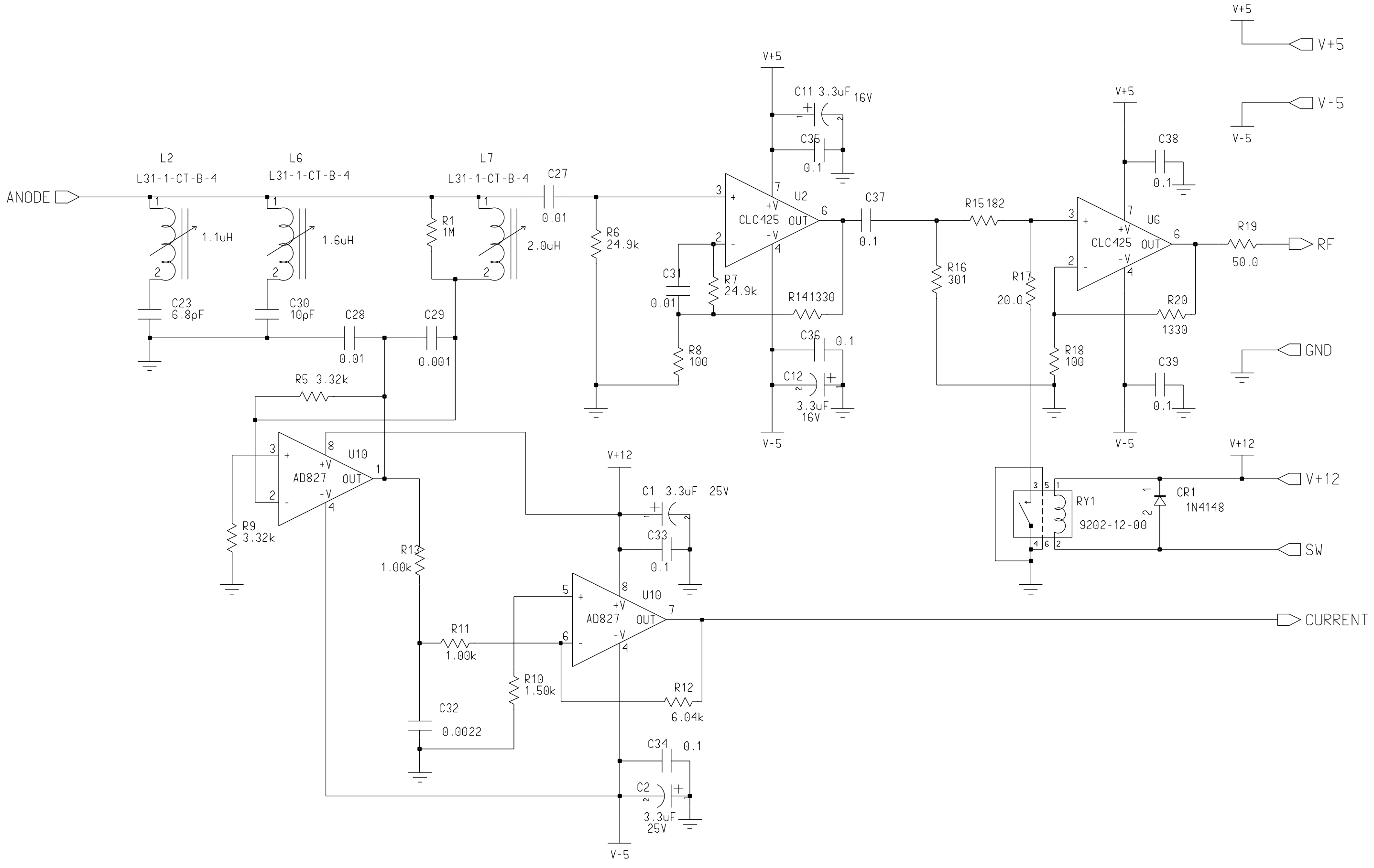

Figure 21: Wavefront sensor head: Channel 1

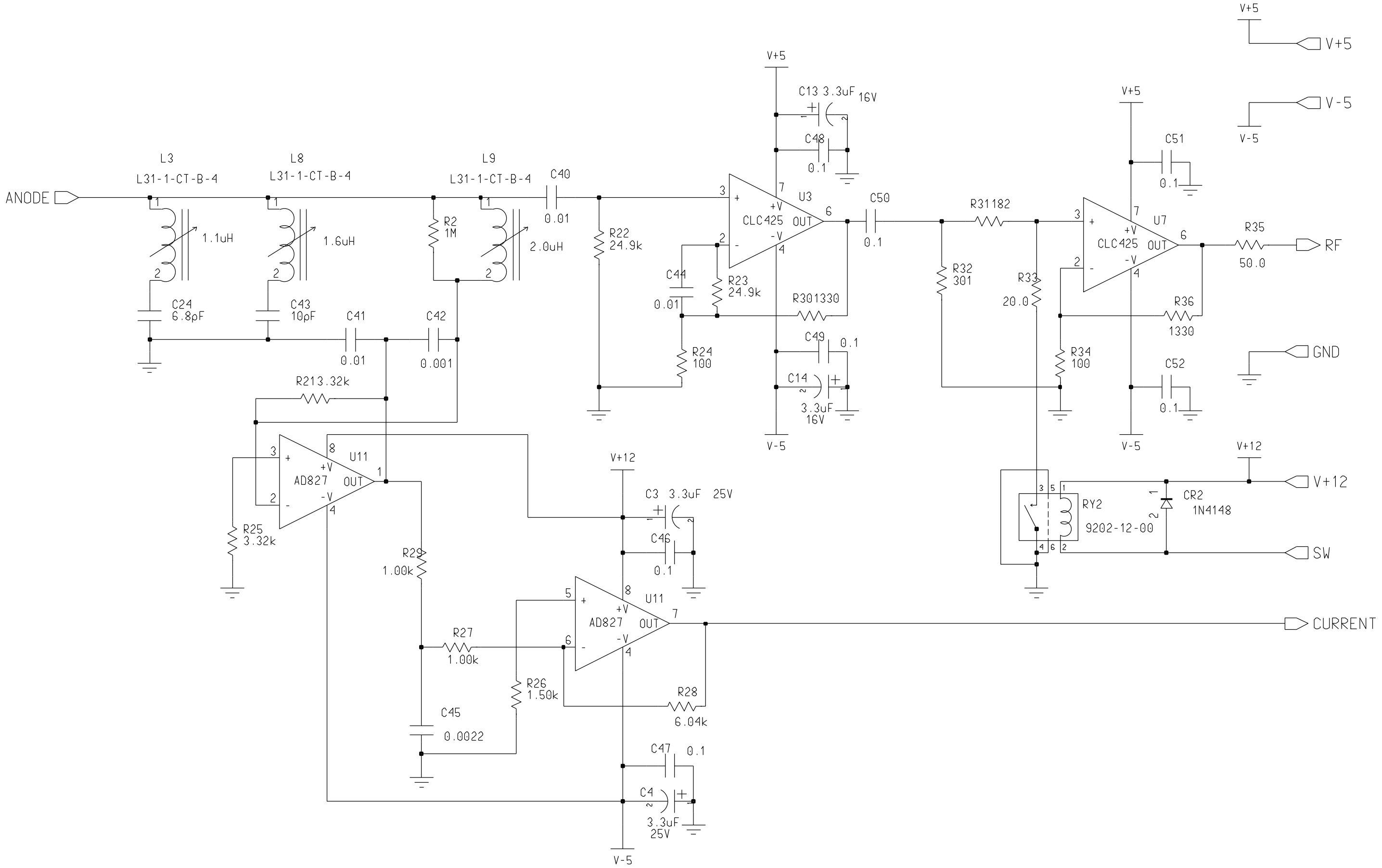

Figure 22: Wavefront sensor head: Channel 2

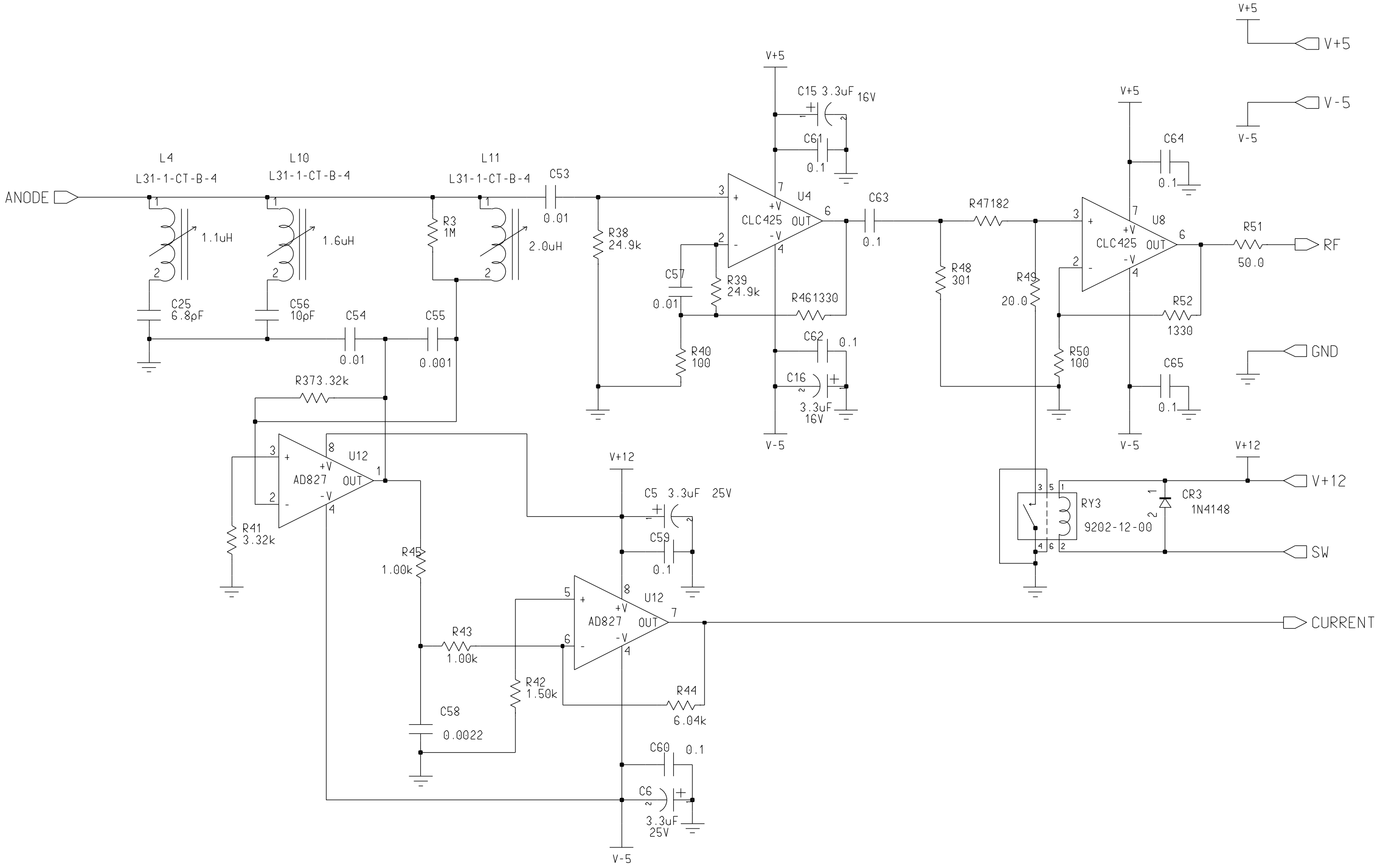

Figure 23: Wavefront sensor head: Channel 3

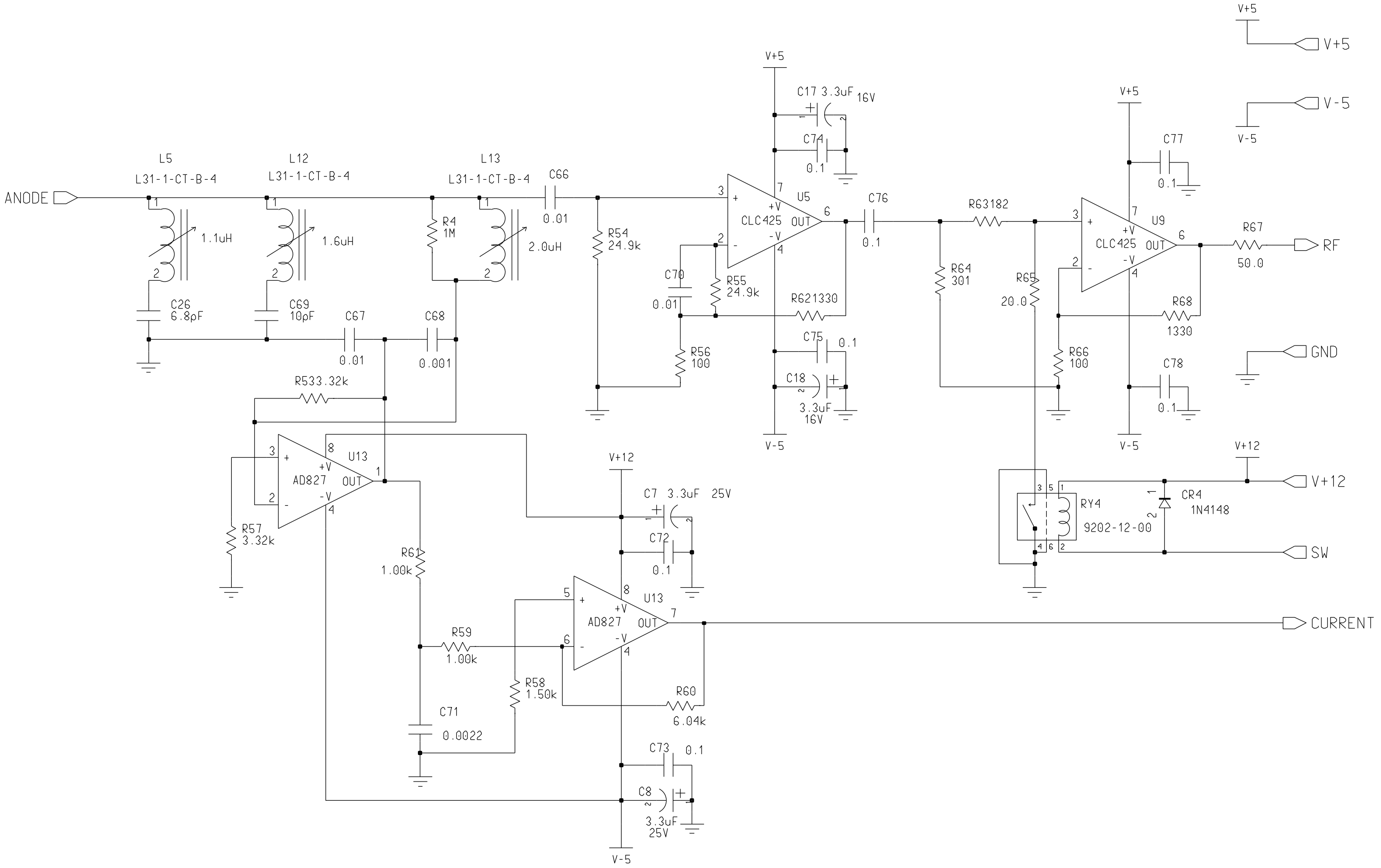

Figure 24: Wavefront sensor head: Channel 4

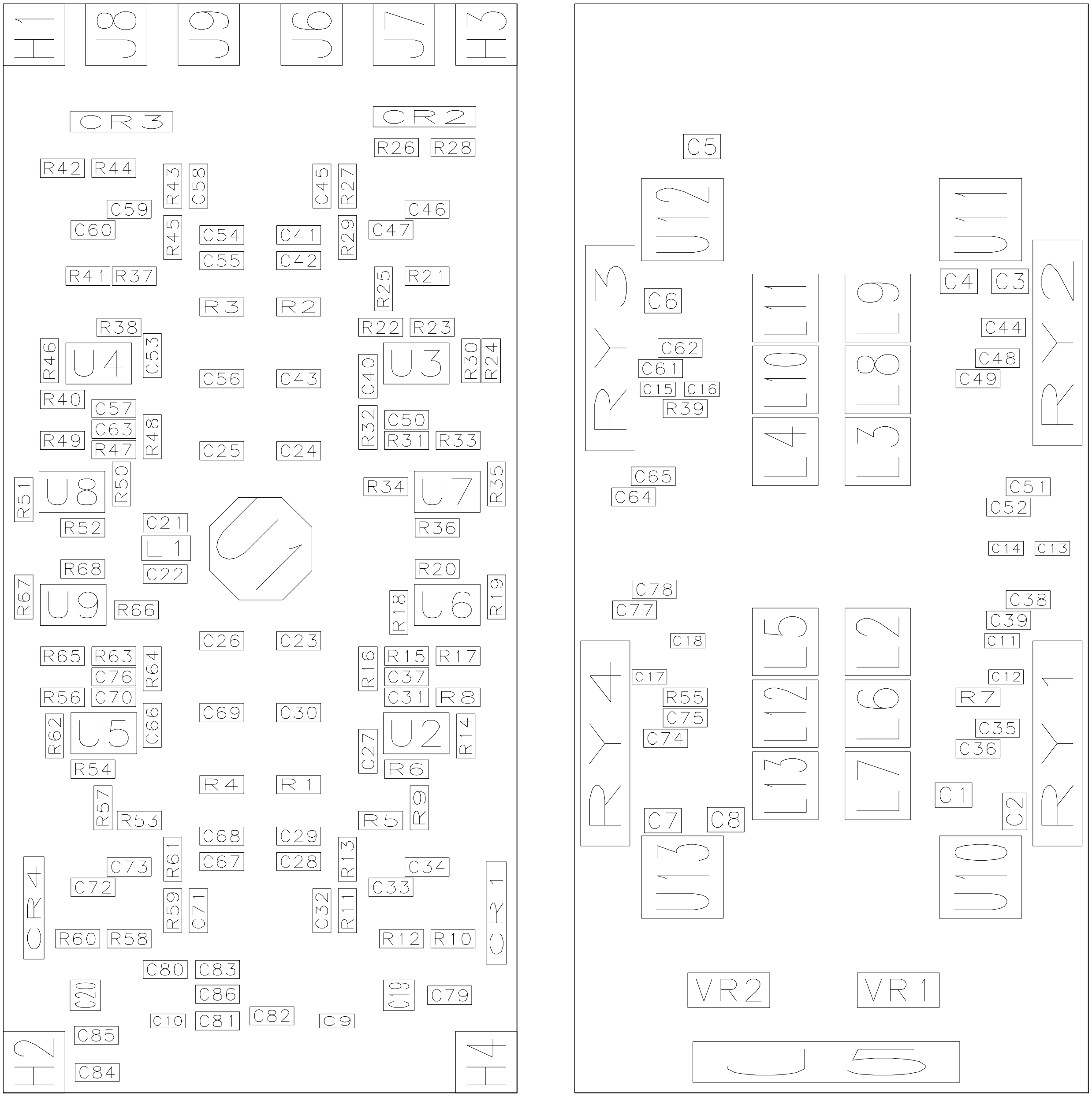

(a) top

(b) bottom

physical board size: 5.3” x 2.5”

Figure 25: Wavefront sensor head: Board layout

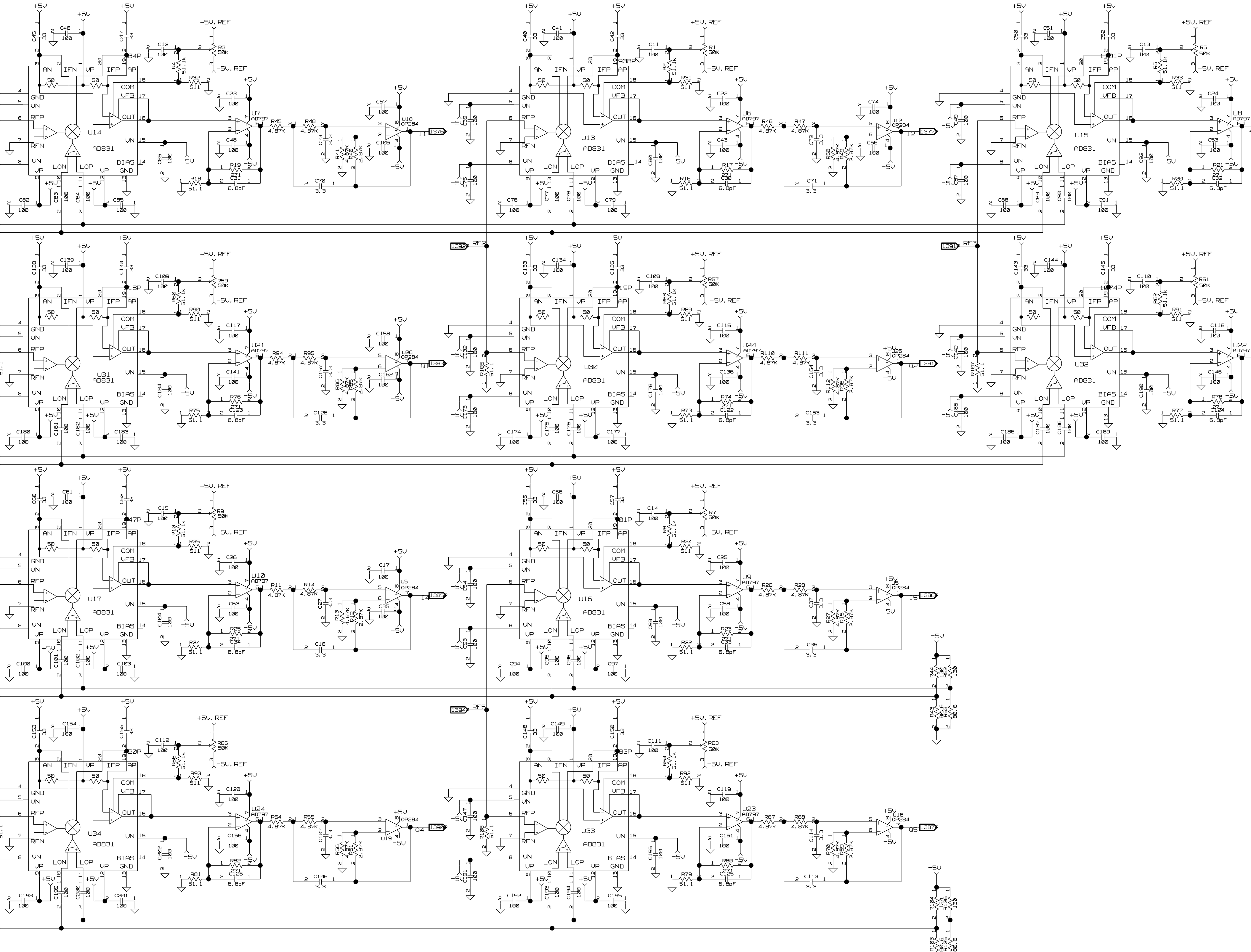

+5V
-5V
+5V.REF
-5V.REF
AN
IFN
VP
IFP
AP
COM
VFB
OUT
GND
VN
RFP
RFN
LON
LOP
BIAS
AD831
AD797
OP284
U14
U13
U15
U31
U30
U32
U17
U16
U34
U33
U7
U18
U6
U12
U8
U21
U26
U20
U22
U10
U5
U9
U24
U19
U23
R3 50K
R1 50K
R5 50K
R59 50K
R57 50K
R61 50K
R9 50K
R7 50K
R65 50K
R63 50K
R4 51.1k
R2 51.1k
R6 51.1k
R32 511
R31 511
R33 511
R45 4.87K
R48 4.87K
R46 4.87K
R47 4.87K
R41 4.87K
R42 2.87K
R18 51.1
R16 51.1
R20 51.1
R19 271
R17 271
R21 271
C31 6.8pF
C30 6.8pF
C32 6.8pF
C70 3.3
C71 3.3
C73 3.3
C72 3.3
C67 100
C74 100
C105 100
C66 100
C12 100
C11 100
C13 100
C23 100
C22 100
C24 100
C48 100
C43 100
C53 100
C45 33
C46 100
C47 33
C40 33
C41 100
C42 33
C50 33
C51 100
C52 33
C82 100
C83 100
C84 100
C85 100
C86 100
C76 100
C77 100
C78 100
C79 100
C80 100
C88 100
C89 100
C90 100
C91 100
C92 100
C39 100
C49 100
C87 100
I1
I2
Q1
Q2
Q4
Q5
I5
1376
1377
1383
1381
1385
1386
1390
1387
1392
1391
1394
RF2
RF3
RF5
R105 51.1
R107 51.1
R108 51.1
R90 511
R89 511
R91 511
R94 4.87K
R95 4.87K
R110 4.87K
R111 4.87K
R76 271
R74 271
R78 271
R75 51.1
R73 51.1
R77 51.1
C123 6.8pF
C122 6.8pF
C124 6.8pF
C128 3.3
C163 3.3
C157 3.3
C164 3.3
C158 100
C162 100
C35 100
C17 100
R35 511
R34 511
R11 4.87K
R14 4.87K
R26 4.87K
R28 4.87K
R25 271
R23 271
R24 51.1
R22 51.1
C34 6.8pF
C33 6.8pF
C16 3.3
C36 3.3
C27 3.3
C37 3.3
R93 511
R92 511
R54 4.87K
R55 4.87K
R67 4.87K
R68 4.87K
R82 271
R80 271
R81 51.1
R79 51.1
C126 6.8pF
C125 6.8pF
C106 3.3
C113 3.3
C107 3.3
C114 3.3
R44 130
R43 80.6
R104 130
R103 80.6
34P
938P
01P
18P
19P
074P
47P
20P
83P

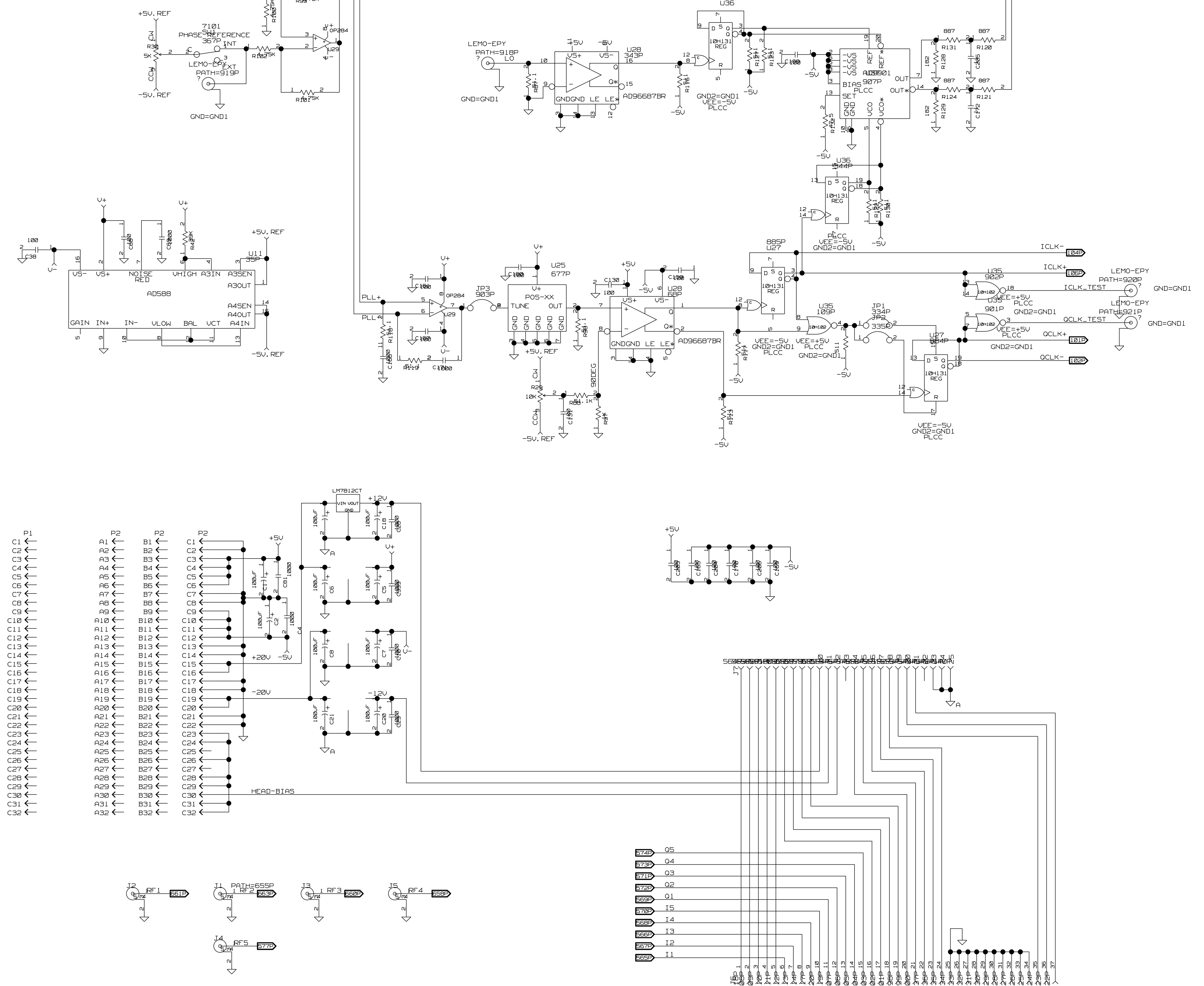

27: Wavefront sensor demodulator: VCO